Nano-crosslinked mesoporous graphene for superior Na-ion storage

Haiyang Fu[1,2,3], Bo Gao[1*], Yuan Qiao[2], Pengshan Lin[1], Zhuang Liu[1], Shiqi Yuan[1], Amor Abdelkader[3], Ali Reza Kamali[2,4*]

1.Key Laboratory for Ecological Metallurgy of Multimetallic Mineral, Ministry of Education, Northeastern University, Shenyang 110819, P.R. China

2.Energy and Environmental Materials Research Centre (E2MC), School of Metallurgy, Northeastern University, Shenyang, 110819, China

3. Faculty of Science and Technology, Bournemouth University, Talbot Campus, Fern Barrow, Poole, BH12 5BB, UK.

4.Department of Materials Science and Metallurgy, University of Cambridge, 27 Charles Babbage Road, Cambridge CB3 0FS

E-mail address: gaob@smm.neu.edu.cn (B. Gao); ali@smm.neu.edu.cn; a.r.kamali@cantab.net (A.R. Kamali)

Abstract

In this study, we present a straightforward method for fabricating nano-crosslinked mesoporous graphene with exceptional sodium-ion storage capabilities. The process involves the mechanochemical preparation of acidic graphene oxide (AGO) powder, followed by the thermochemical exfoliation of AGO to produce thermochemically exfoliated graphene (TEG) characterized by a layer spacing of 0.362 nm, an increased specific surface area, and a distinctive nano-crosslinked porous structure. Specifically, TEG prepared at 400 °C (TEG-400) exhibits remarkable Na-ion storage performance, showcasing an initial capacity and coulombic efficiency of 402 $mAh \cdot g^{-1}$ (100 $mA \cdot g^{-1}$) and 86%, respectively. Notably, TEG-400 demonstrates outstanding cyclic stability with a reversible capacity of 281 $mAh \cdot g^{-1}$ after 300 cycles at 200 $mA \cdot g^{-1}$ and 219 $mAh \cdot g^{-1}$ after 1000 cycles at 2000 $mA \cdot g^{-1}$. The superior electrochemical performance of the TEG-400 electrode can be attributed to its large specific surface area (517 $m^2 \cdot g^{-1}$), high pore volume (2.29 $cm^3 \cdot g^{-1}$), and introduced defects, providing ample active sites for the rapid storage of sodium ions through surface adsorption into the defect sites. This research offers insights for advancing the development and design of next-generation high-performance sodium-ion battery electrode materials.

Keywords: thermochemical exfoliation; nano-crosslinked structure; porosity; coulombic efficiency; Na-ion storage; anode

1 Introduction

The availability of efficient and low-cost energy storage technologies is crucial for widely utilizing of renewable energy sources [1,2]. The escalating demand for energy storage devices, notably Li-ion batteries, has been substantial, fueled by the increasing reliance of a growing population on electronic devices and electric vehicles. However, this heightened demand is expected to strain global lithium resources, potentially resulting in scarcity and subsequent price increases, rendering them progressively less affordable for future developments [3]. Hence, a key challenge lies in developing alternative energy storage systems that transcend Li-ion technology. Leveraging the similar physical and chemical properties of sodium and lithium, Na-ion batteries (SIBs) emerge as highly promising alternatives to their Li-ion counterparts, where sodium is far more abundant than lithium, enhancing the feasibility and sustainability of SIBs [4-7]. It's noteworthy that SIBs share a similar mechanism with LIBs, based on which, in the charging phase, the cathode undergoes dissociation, allowing Na-ions to traverse the electrolyte to the anode; and simultaneously, electrons move through the external circuit from the cathode to the anode. Conversely, during discharge, the anode experiences dissociation, and Na-ions return to the cathode via the electrolyte, while the electrons travel through the external circuit from the anode to the cathode, enabling the battery to supply power to the external circuit [8]. Nevertheless, while lithium-ions can be reversibly intercalated into graphite to form LiC_6, offering a specific capacity of 372 $mAh \cdot g^{-1}$ [9], the downside is that graphite can only be sodiated to form NaC_{64}, resulting in a much lower capacity of approximately 35 $mAh \cdot g^{-1}$ [10,11]. Since the radius of Na-ion (0.102 nm) is much larger compared to the Li-ion radius (0.076 nm) [12], the insertion of Na-ions into graphitic structures requires a wider layer spacing

than that of graphite (0.33 nm) and associated with more significant volume expansion [13, 14]. To enhance Na-ion storage efficiency, a range of carbonaceous materials beyond graphite has been explored, including EG [15], hard carbon [16], soft carbon [17], carbon nanotubes [18], hollow carbon nanospheres [19], porous carbon [20], graphene [21], and amorphous nitrogen-, boron-, and phosphorus-doped graphene [22-24]. Among them, graphene nanonetworks hold particular significance due to their ability to shorten Na-ion transport distances, thereby enhancing electrode/electrolyte interfaces and charge transfer kinetics [25].

Since the discovery of graphene in 2004 [26], various chemical methods have been employed to craft graphene structures for use as anodes in SIBs. For instance, Tong et al. [27] developed a porous carbon (MPC) material through a demoulding method, utilizing spherical nano-SiO_2 as a pore-forming agent, gelatine and polytetrafluoroethylene (PTFE) as carbon sources. The MPC anode, when tested in a Na-ion half-cell, demonstrated an impressive initial coulombic efficiency (ICE) of up to 83%, and a high-rate capability, achieving a capacity of 208 $mAh \cdot g^{-1}$ at a current density of 5 $A \cdot g^{-1}$. Such porous carbons could also be fabricated by the incorporation of cobalt- germanium hydroxide through hydrothermal synthesis, providing a reversible capacity of 416 $mAh \cdot g^{-1}$ after 100 cycles at a 100 $mA \cdot g^{-1}$, 206 mA $h \cdot g^{-1}$ at a current density of 2000 $mA \cdot g^{-1}$ [28]. Other works include reduced graphene oxide doped with boron-cobalt nanorods, demonstrating a capacity of 444 $mAh \cdot g^{-1}$ after 50 cycles at 100 $mA \cdot g^{-1}$, and exceptional rate performance, achieving 270.5 $mAh \cdot g^{-1}$ at 2000 $mA \cdot g^{-1}$ [29]. Additionally, polycyclic aromatic hydrocarbons synthesized through the pyrolysis of quinacridone and subsequent thermal polymerization exhibit a capacity of 247 $mAh \cdot g^{-1}$ at 100 $A \cdot g^{-1}$ after 200 cycles, and 134 $mAh \cdot g^{-1}$ at 5000 $mA \cdot g^{-1}$ after 1000 cycles [30]. Despite the observed

enhancements in the electrochemical properties of these porous carbon composites, the related preparation methods often involve cumbersome conditions. Consequently, there is a critical need for simpler techniques to efficiently produce high-quality graphene materials with desirable characteristics and achieve even greater electrochemical performances.

This study, explores a thermochemical exfoliation technique to prepare a graphene material (TEG-400) with modified oxygen functional groups, surface structure, carbon layer spacing, pore volume and specific surface area. These enhancements result in abundant electrochemically active sites, facilitating efficient sodiation and desodiation processes. To achieve this objective, we synthesize acidic graphene oxide (AGO), a distinctive variant of conventional graphene oxide. Unlike its counterpart, AGO is a yellowish-brown powder with reduced surface hydrophilic groups. Furthermore, AGO can be conveniently isolated from the suspension through precipitation, deviating from the traditional centrifugation method. We further apply ball milling on AGO to prevent the agglomeration of flakes, and perform thermochemical exfoliation to create nano-crosslinked porous graphene featuring defect sites. Additionally, the augmentation of graphene layer spacing impedes π-π bond stacking. As a result, TEG-400 exhibits a large specific surface area (517 $m^2 \cdot g^{-1}$), a mesoporous structure bearing a pore volume of 2.29 $cm^3 \cdot g^{-1}$, and the electrical conductivity of around five orders of magnitude higher than that of AGO. Furthermore, the existence of defects in the graphene nano-crosslinks enhances the electrochemical properties of the material. This is evidenced by an exceptionally high initial capacity of 414 $mAh \cdot g^{-1}$ at a current density of 200 $mA \cdot g^{-1}$, accompanied by an outstanding first-cycle coulombic efficiency of 86%. Moreover, the material exhibits outstanding capacity retention, sustaining a capacity of 219 $mAh \cdot g^{-1}$ at 2000

$mA \cdot g^{-1}$ after 1000 cycles. This impressive durability can be ascribed to the nano-crosslinked structure, elevated pore volume, and specific surface area of the material, prompting the reversible electrochemical sodiation at graphene surface defects and within the pore structure.

2 Experimental

2.1 Materials

The raw materials employed in this study comprised graphite powder (1 μm, 99.95%), sulfuric acid (98%), potassium permanganate (>99.0%), nitric acid (65%), and hydrogen peroxide (30%). These chemicals were procured from Sigma-Aldrich and utilized without additional purification. Deionized water was used in the preparation of all solutions.

2.2 Synthesis of acidic graphite oxide (AGO）

The modified Hummers method [31,32] underwent further modification to produce acidic graphite oxide powder (AGO). Initially, 2.0 g of graphite powder was added into a 500 mL beaker containing a mixed solution of 220 mL of sulfuric acid and nitric acid, with a volume ratio of 10:1. Subsequently, 12.0 g of potassium permanganate was incrementally added to the beaker in four portions at 10-minute intervals. The mixture was then heated at 50, 60, and 90°C for durations of 40 minutes, 6 hours, and 30 minutes, respectively.

The mixture was then allowed to cool naturally and diluted with 5 times deionized water, followed by adding 25 mL of H_2O_2 to the mixture, leading to the preparation of an orange-yellow solution. This solution was then diluted with deionized water until pH ≈ 6 was achieved. Then, a yellow-brown colloidal mass was precipitated by leaving the suspension for 3h, which

subsequently separated by removing the upper layer of the liquid. The sample was then freeze-dried to obtain AGO, as a yellow-brown powder. Fig. S1 illustrates various samples explained above. The specific color of the AGO is due to the presence of oxygen containing groups on its surfaces, as commonly be found in oxidized carbon nanomaterials [33,34].

2.3 Synthesis of thermochemically exfoliated graphene（TEG）

To prepare the thermochemically exfoliated graphene (TEG), the AGO powder was transferred into the ball-milling jars and subjected to ball milling using a micro vibrating mill device (MSK-SFM-12M, Hefei Kejing) for 30 minutes. Subsequently, the ball-milled AGO samples (1g) underwent thermochemical exfoliation in a tube furnace. Initially, argon protective gas was passed through the tube for 10 minutes. The temperatures were then set at 100, 200, 300, 400, and 500°C, and the heating process was executed at a rate of $5°\cdot min^{-1}$ with a dwell time of 2 hours under a continuous flow of argon gas. The resulting samples were designated as TEG-100, TEG-200, TEG-300, TEG-400, and TEG-500, respectively. Fig. 1 illustrates the preparation method as detailed above.

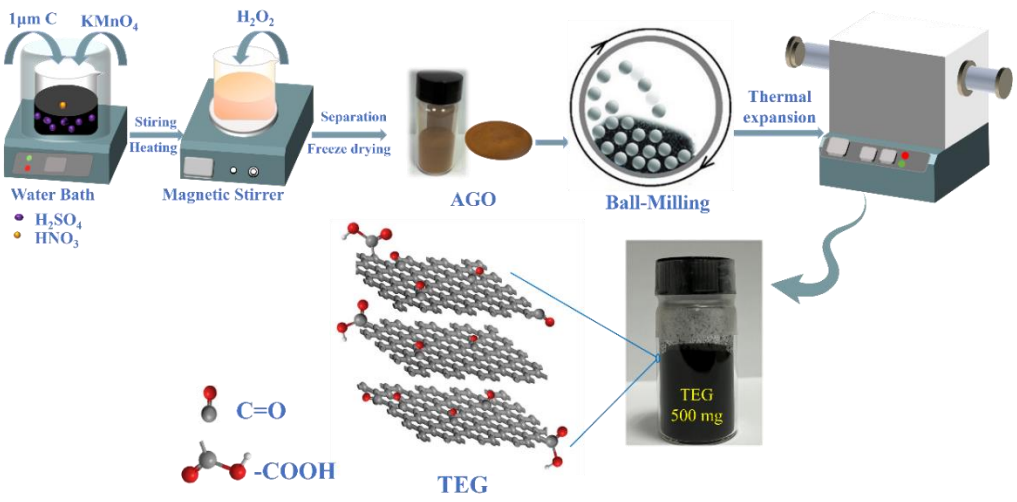

Fig. 1. Illustration of the synthesis process of thermochemically exfoliated graphene (TEG).

2.4 Characterizations

Microscopy studies were conducted using a field emission scanning electron microscope (SEM, Zeiss Ultra Plus) equipped with an energy dispersive X-ray (EDS) detector. TEM micrographs were obtained on a JEM-2100F instrument. X-ray powder diffraction (XRD) analysis was carried out on a Rigaku XRD Analyzer (smartlab) with Cu- K_α radiation (λ= 1.54056 Å) and the scanning step of 0.02° in the range 2θ = 5°-65° at the scanning speed of 5° min^{-1}. Raman spectroscopy was carried out using a laser Raman spectrometer (HR800) at a wavelength of 633 nm (He-Ne laser). Fourier transform infrared (FTIR) spectra were recorded on a Bruker VERTEX70 spectrometer from 4000 to 500 cm^{-1} using KBr pellet. X-ray photoelectron spectroscopy (XPS) was performed on a Thermo Scientific K-Alpha instrument using a non- monochromatic Al-K_α source (1486.6 eV) in a UHV chamber. The area of the samples prepared for the analysis was 400 × 400 μm^2. Advantage software was used for background subtraction (Shirley-type background) and curve-fitting analyses, and calibrations were performed using the aliphatic component of the C1s peak at 284.8 eV; whereas line synthesis of the elemental spectra was performed by Gauss-Lorentz (70:30) curve-fitting. The specific surface area was calculated from the BET plots obtained by N_2 adsorption/desorption isotherms. The model used for the density test was ZS-102 vibration densitometer with 2,000 times / (200 n / min) / Amplitude 3 mm. The Malvern Zetasizer Nano ZS ZEN3600 instrument was used to test the nanoparticle size. Yongpeng YP2511 DC resistance tester was used to measure resistivity/conductivity of materials using equations (1) and (2).

$$\rho = \frac{RS}{L} \qquad (1)$$

$$k = \frac{1}{\rho} \qquad (2)$$

where ρ is the resistivity ($\Omega \cdot m$), S is the cross-sectional area (m^2), R is the resistance value (Ω), L is the wire length (m) and k is the conductivity ($S \cdot m^{-1}$).

2.5 Electrochemical measurements

The electrochemical performance of the samples was evaluated using a two-electrode half-cell configuration. For the electrode fabrication, a mixture of the active material (TEG), conductive carbon (C45, Tianjin Aiweixin Chemical Technology) and binder (Polyvinylidene fluoride, PVDF, Shanghai Macklin Biochemical Technology) with a weight ratio of 7:2:1 were ground homogenously by the application of N-Methyl pyrrolidone (NMP) as the solvent. The resultant slurry was coated on a copper foil with a thickness of around 200 μm using the doctor blade method, and subsequently dried at 80 °C for 12 h in a vacuum oven. The mass loading of the active material was around 0.7 $mg \cdot cm^{-2}$. Typical CR2032 coin half-cells were prepared in which metallic Na was used as both the counter and reference electrode. Then, coin-type half-cells (CR 2032) were assembled using metallic sodium as the counter electrode, 1.0 M $NaCF_3SO_3$ in diglyme (Suzhou Duoduo Chemical Technology) as the electrolyte, and glass microfiber (Whatman, 1823025) as the separator. The half-cells were assembled in an argon-filled glove-box (Mikrouna) with O_2 and H_2O levels of less than 0.1 ppm. The cells were allowed to equilibrate for 10 h at room temperature before electrochemical tests. Galvanostatic charge-discharge measurements were performed at 0.01-3.0 V (25 °C) using a LAND battery test system. The electrochemical reactions taking place in the electrodes were evaluated by cyclic voltammetry (CV) performed using a CHI 660E electrochemical workstation at the scan rate and voltage range of 0.3 $mV \cdot s^{-1}$ and 0.01-3.0 V vs Na/Na^+, respectively. Electrochemical

impedance spectroscopy (EIS) was performed in the frequency range 100 kHz - 0.01 Hz, and the spectral analysis was carried out using Zview software.

3 Results and discussion

3.1. Structural and morphological characterization of TEG-X

TEG-X (X=100, 200, 300, 400 and 500) samples were prepared using the method shown in Fig. 1. Figs. S2a (Supporting Information) reveal the morphological characteristics of the TEG-100 material, displaying a significant folded morphology without a clearly evident layered structure. This observation is due to relatively low temperature of the thermal process, preventing an efficient volume expansion and thermal exfoliation of the graphene material in TEG-100. In contrast, the thermally exfoliated graphene TEG-200 (Fig. S2b) begins to exhibit a layered structure that adheres closely, providing evidence for the initiation of volume expansion and thermal exfoliation in this sample. This layered configuration further evolves in TEG-300 (Fig. S2c), developing of a discernible pore structure. However, as depicted in Fig. S2d, the layered structure becomes imperceptible in TEG-500, presenting a closely stacked arrangement instead. An augmented layered structure, affording a substantial specific surface area and a porous framework in TEG-X, can contribute to enhanced electrochemical properties, as will be discussed in this paper.

Table S1. Vibratory density testing of TEG-400

Sample	Vibratory density $g \cdot cm^3$	Average vibratory density $g \cdot cm^3$
TEG-400	0.018	0.0183
	0.017	
	0.020	

Compared to alternative TEG-X samples, TEG-400 shows a more distinct nano-crosslinked layered structure, as shown in SEM micrographs of Figs. 2a and 2b. The oxygen content was found to be 7.79% by EDS spectroscopy of TEG-400, as depicted in Fig. S3a. This sample was determined to be ultra-lightweight, with an average tap density of only 0.0183 $g \cdot cm^{-3}$ (Table S1), considerably lighter than the values reported in the literature for alternative graphene materials, by more than an order of magnitude. For instance, the electrochemical exfoliation of graphite in molten salt [14] can result in the production of graphene nanosheets with an apparent density of approximately 0.24 $g \cdot cm^{-3}$, significantly lower than that of graphite powder (1.60 $g \cdot cm^{-3}$) [35]. The low apparent density of TEG-400 confirms its highly layered and porous nano-crosslinked structure, improving the electrochemical performance and stability of the graphene material.

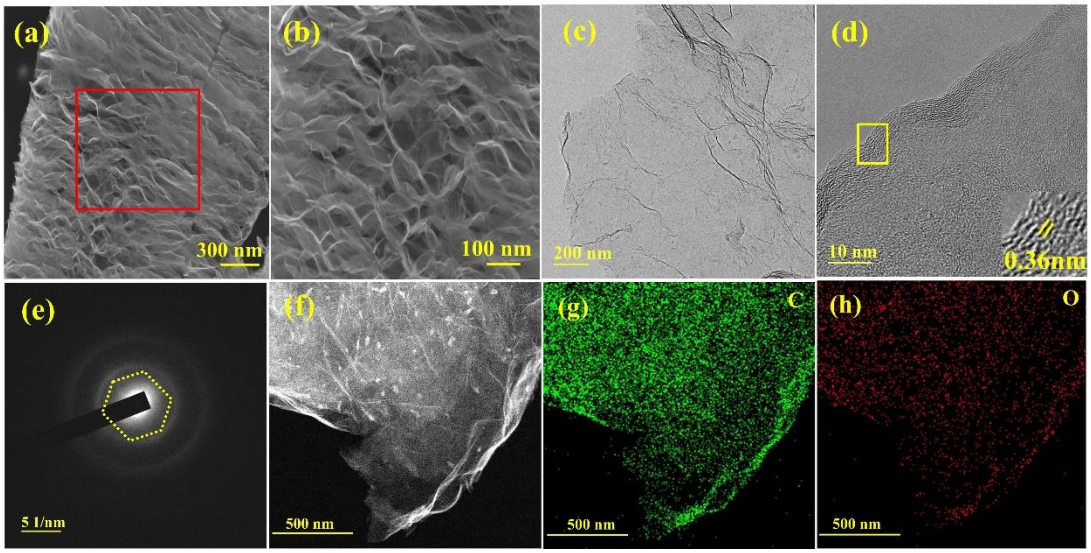

Fig.2. Microscopic features of TEG-400: (a) SEM and (b) magnified SEM micrographs. (c) bright-field TEM, (d) HRTEM, (e) SAED, (f) dark-field TEM, and (g, h) EDS map analysis of recorded on the graphene.

The morphological features of TEG-400 were further investigated using TEM, revealing a muslin-like morphology of the graphene material, as shown in Fig. 2c. The thin sheet layer

of the graphene material and its expansive specific surface area contribute favorably to charge transfer within the electrode composed of the material. The high-resolution TEM (HRTEM) image of TEG-400 (Fig. 2d and the inset of the figure) distinctly reveals the striated structure of the nanomaterial, with a layer spacing of 0.36 nm. The electron diffraction pattern captured on graphene (Fig. 2e) illustrates the presence of defined diffraction spots corresponding to the hexagonal lattice structure of graphene. Applying the thermochemical exfoliation technique led to the exfoliation of stacked graphene sheets. The nanostructured material obtained could potentially enhance the electrochemical properties of the material. Based on the dark-field TEM micrograph in Fig. 2f and the elemental mapping analysis depicted in Figs. 2g and 2h, the presence of uniformly distributed oxygen on carbon is evident. During the thermochemical exfoliation step (Fig. 1), a significant quantity of oxygen-containing groups is eliminated from graphene. The oxygen content of TEG-400 was determined to be 5.21 % through EDS analysis, as depicted in Fig. S3b. This corresponds to the XPS results discussed later.

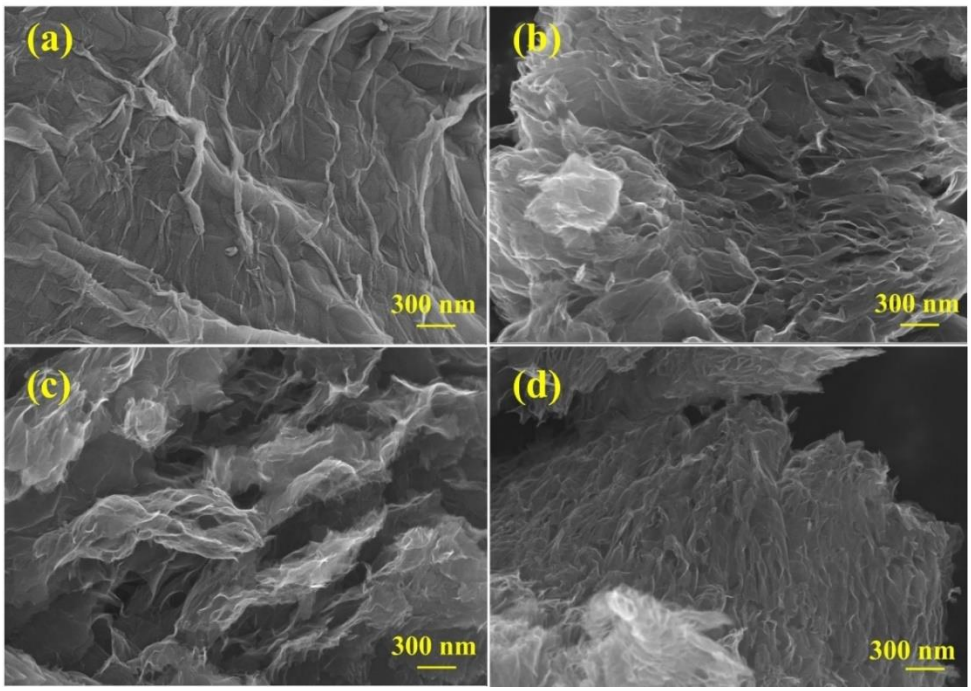

Fig.S2. SEM micrographs of (a) TEG-100, (b) TEG-200, (c) TEG-300 and (d) TEG-500.

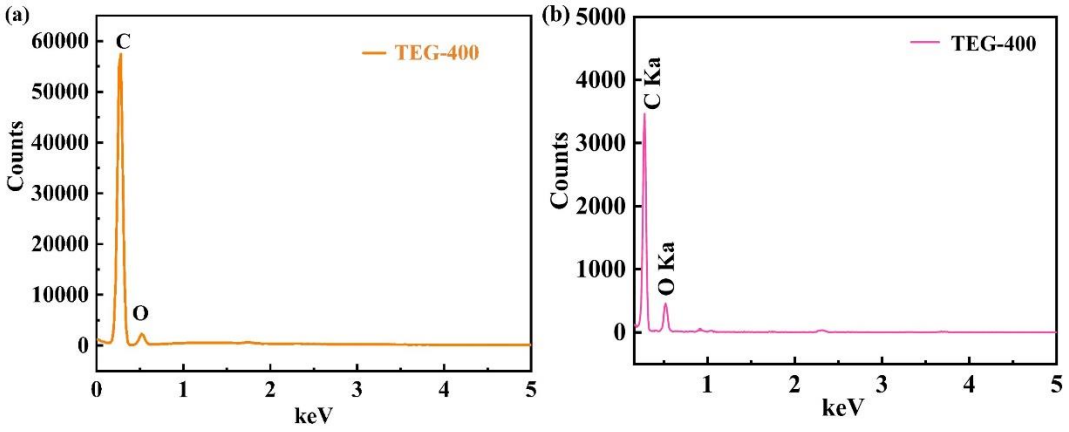

Fig. S3. EDS spectrum of TEG-400 recorded using (a) SEM and (b) TEM micrographs shown in Fig. 2.

In this investigation, TEG materials were synthesized through the thermochemical exfoliation of ball-milled AGO. The X-ray diffraction patterns for both AGO and TEG-X samples are depicted in Fig. 3a. Notably, the (002) diffraction peak, a distinctive feature in graphitic carbon [36], is evident at $2\theta \approx 26°$ in the TEG samples. In contrast, the predominant peak in AGO emerges at $2\theta \approx 11.2°$, which is attributed to the incorporation of hydroxyl (-OH), C-O, C=O, and carboxyl (O-C=O) groups into the structure of the graphene oxide during oxidation [37]. The X-ray diffractogram in Fig. 3a highlights the blue shaded region, signifying the (002) reflection corresponding to the hexagonal carbon structure in thermally exfoliated graphene samples, positioned at $2\theta \approx 26°$. This observation indicates the successful reduction of AGO at temperatures equal or greater than 200 °C. In TEG-X, thermochemical exfoliation effectively diminishes the high degree of oxidation in graphene flakes, yet introduces structural defects due to the persistence of carbon atoms with sp^3 hybridization within the material. This phenomenon is also responsible for the shift in the 2θ position of the (002) reflection.

In addition, the strongest peak of TEG-100 at $2\theta \approx 11.5°$ corresponds to the (001) crystal plane, while the weak diffraction peak appearing at $2\theta \approx 42.3°$ is a characteristic peak of graphene and corresponds to the (100) crystal plane [38]. These indicate the presence of

oxygen-functional groups in the carbon layer structure, confirming that the reaction temperature of 100 °C is not sufficient to reduce graphene. Table 1 illustrates the calculated graphene layer spacing and layer thickness using the semi-empirical Bragg formula (Equation 3) and the Scherer formula (Equation 4), respectively [39]:

$$2d\ sin\ \theta = n\lambda \quad (3)$$

$$L = \frac{K \cdot \lambda}{\beta \cdot \cos\theta} \quad (4)$$

where n is the diffraction order, λ is the characteristic spectral wavelength of the X-ray tube target material, and K is 0.89. β is the half-peak of the measured samples.

Table 1. Layer spacing (d) and slice thickness (L) of AGO and TEG-X samples

Samples	Layer spacing d/nm	Slice thickness L/nm
AGO	0.797	9.155
TEG-100	0.763	7.938
TEG-200	0.356	0.850
TEG-300	0.358	0.829
TEG-400	0.362	0.775
TEG-500	0.355	0.886

Notably, the layer spacing is an important factor determining the Na-ion storage performance. Although the layer spacing is AGO is large (0.797 nm), the electrical conductivity of this sample is very poor (Table S5), suggesting the presence of a large number of surface oxygen containing groups in this sample. The layer spacing of AGO and TEG-100 is approximately 0.8 nm, which is reduced to 0.362 nm after thermochemical exfoliation at

400 °C (TEG-400), providing further evidence of the substantial reduction in oxygen-containing functional groups. Furthermore, employing the Scherer formula (Equation 4), the sheet thicknesses of graphene TEG-X samples, prepared through the thermochemical exfoliation method, are calculated as 7.938, 0.850, 0.829, 0.775, and 0.886 nm, respectively. According to Table 1, TEG-400 has the largest layer spacing of 0.362 nm as well as the smallest sheet thickness (0.775 nm), facilitating the transportation of Na-ions through the graphene muslin structure, improving the Na-ion storage performance of the sample. This observation highlights that the thermochemical exfoliation is capable of a distinct nano-network thin layer structure and a substantial layer spacing, contributing significantly to enhanced electrochemical performance.

Fourier-transform infrared spectroscopy (FTIR) provides insight into the structural characteristics of AGO and TEG-X materials. The FTIR spectra for AGO and TEG-X are depicted in Fig. 3b. As evidenced, the thermochemical exfoliation process results in the reduction of AGO, leading to the elimination of oxygen-containing functional groups and the restoration of the sp^2 structure. In the AGO and TEG-100 spectra, the peaks corresponding to water molecules, carbonyl (C=O), carbon-carbon double bonds (C=C), carboxyl (O-C=O), and C-OH are observed at 3446, 1735, 1612, 1217, and 1053 cm^{-1}, respectively [39, 40]. Comparatively, in TEG-200, TEG-300, TEG-400, and TEG-500 spectra, a significant reduction in water molecules is evident compared to AGO and TEG-100. The green region in Fig. 3b indicates the restoration of carbon-carbon double bonds (C=C) and the relative elimination of the stretching vibrational peak associated with the C=O bond. Notably, the absence of the C-OH bond suggests the reduction of graphene oxide into graphene. It should be considered that

TEG-100 exhibits a spectrum akin to that of AGO, indicating that 100 °C is insufficient for the complete reduction of graphene, consistent with XRD results.

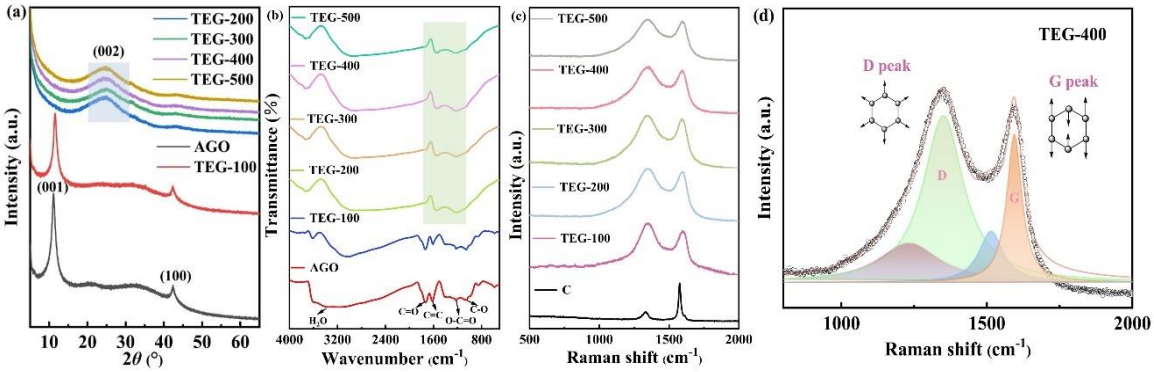

Fig.3. (a) XRD patterns and (b) FT-IR spectra of AGO, TEG-100, TEG-200, TEG-300, TEG-400 and TEG-500 powders. (c) Raman spectra of thermochemically exfoliated graphene samples and graphite. (d) Raman spectra of TEG-400 with Lorentz fitting.

According to fig. 3b, the TEG-400 spectrum reveals a weakened conjugated structure, suggesting that covalent bonds in thermally exfoliated graphene are partially broken, resulting in the presence of graphene with low crystallinity. This phenomenon contributes to a reduction in the value of the electrical conductivity of nano-crosslinked graphene. Nonetheless, the outstanding mesoporous structure, substantial specific surface area, increased layer spacing, and the presence of few layers of muslin-like nano-crosslinked graphene collectively play a pivotal role in augmenting electrochemical performance.

Raman spectroscopy serves as a powerful analytical tool for characterizing sp^2 [41] and sp^3 [42] hybridized carbon materials, offering insights into the modifications brought about by variations in the yarn-like structure of carbon nanonetworks within electrode materials [43]. According to Fig. 3c, in the graphite sample, two characteristic bands are discernible at ~1339 cm^{-1} and ~1589 cm^{-1}, attributed to the Raman D and G peaks commonly appeared in graphitic

materials [44]. The D band is associated with disordered and defective carbon, while the G band corresponds to ordered sp^2 graphitic carbon [45]. In contrast, the D and G peaks of TEG-400 are positioned around 1343 and 1593 cm^{-1}, respectively, with the blue shifted G peak exhibiting a reduced intensity, indicative of alterations in the graphite lattice structure. The results indicate a significant reduction in the size of the sp^2 domains occurred due to the exfoliation process [46,47]. Notably, in the Raman spectra of graphene materials prepared through the chemical and thermochemical exfoliation techniques, low-intensity 2D peaks are typically observed, attributed to the disruption of the graphene layer via the redox process [28, 48-50]. Due to the high structural defect, the Raman spectra of TEG-X do not show 2D peaks. On the other hand, the Raman I_D/I_G ratio can serve as a measure of disorder in graphene materials. As depicted in Fig. 3c, the I_D/I_G ratios for graphite, TEG-100, TEG-200, TEG-300, TEG-400, and TEG-500 are 0.192, 1.290, 1.172, 1.140, 1.120, and 1.156, respectively. As can be seen, the defects level of TEG does not considerably affect by the thermal treatment process. This observation can be elucidated by the fact that during the thermochemical exfoliation treatment, while a fraction of oxygen-containing groups is removed from the surfaces of AGO, it can still leave structural defects behind.

It should be mentioned that structural disorder in carbon materials provides additional sites for accommodating sodium ions, thereby enhancing the specific capacity of the cell. On the other hand, it also increases irreversible capacity [51, 52]. Therefore, excessive defect introduction can lead to poor electrochemical performance. However, TEG-400, can provide a balance between the values of disorder, surface area and pore volume to exhibit an optimum level of sodium ion storage sites, thus electrochemical performance, as will be discussed herein.

Concurrently, the nanoparticulate nature of TEG-400 and its graphene nanonetwork muslin structure offer swift channels for ion migration.

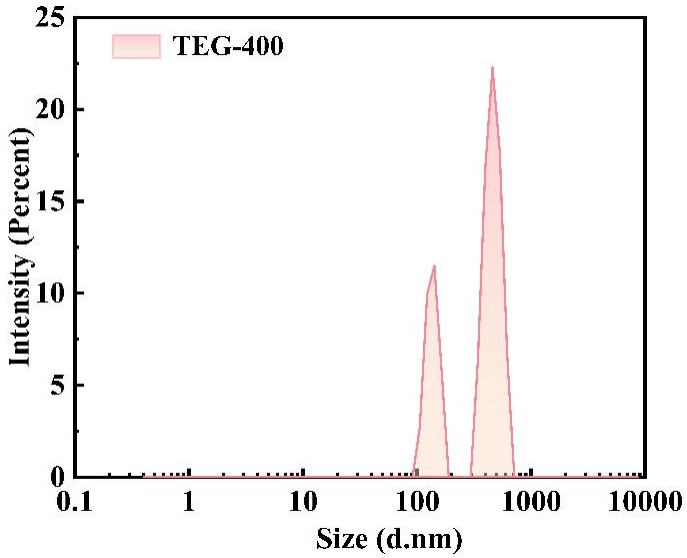

Fig. S4. Particle size distribution of TEG-400 material by intensity.

Raman spectroscopy can be used to measure the ratio of carbon sp^2/sp^3 [53]. According to Fig. 3d, the Lorentzian fitting performed on the Raman spectrum of TEG-400 reveals peaks corresponding to sp^2 and sp^3 hybridized carbon. The fitted curves at 1350 and 1594 cm^{-1} can be attributed to the sp^2, while those for sp^3 are fitted at 1231 and 1514 cm^{-1}. The integral area intensity ratio of sp^2 to sp^3 is approximately 2.45, indicating that sp^2 carbon constitutes around 71% of the heterogeneous carbon, with sp^3 carbon accounting for the remaining 29%. Tuinstra and Koenig [46] found an inverse relationship between the in-plane grain size (L) and the Raman I_D/I_G for graphene materials, so that a larger value I_D/I_G could be correlated with a smaller grain size, providing evidence that the decrease in grain size introduces long-range periodic disruptions [54]. The flake size distribution of TEG-400, as determined through laser light scattering techniques, is illustrated in Fig. S4. The distribution reveals two prominent

peaks at 136.5 nm (30%) and 466.5 nm (70%), indicating an average flake size of 578 nm.

3.2. Surface characterization of AGO and TEG-X

We conducted a comprehensive analysis of the surface functional groups present in AGO and TEG-X samples using XPS, and the findings are presented in Fig. 4. The results are employed to shed further light on to the influence of thermochemical process on mechanism. The XPS spectrum of the AGO sample (Fig. S5) reveals a notable concentration of oxygen-containing functional groups. Additionally, as indicated in Table S2, TEG-100 retains a large number of oxygen-containing groups, proving once again that 100°C is not sufficient to fully thermally exfoliate the graphene material. This is consistent with the SEM illustration (Fig. S2a) which does not show a layered structure. As the result, BET results show that TEG-100 has the smallest specific surface area and pore volume among all the samples (Table 2). XPS (Table S2) and SEM (Fig. S2b) suggest that during the thermochemical stripping process of TEG-200, a large number of hydroxyl, carbonyl and carboxyl groups can be removed forming gas species such as CO, CO_2 and H_2O [55]. This phenomenon leads to the structural delamination, increasing the values of specific surface area and porosity. According to Fig. S2, although the delaminated morphology can be observed in TEG-200, TEG-300, TEG-400 and TEG-500, this effect is less obvious in TEG-500 due to restacking occurring at the higher temperature of 500 ºC. This observation can be confirmed by Table S2 confirming that that the oxygen content of TEG-500 (6.62 at %) has increased in comparison to that of TEG-400 (5.51 at%). The latter also exhibits the most obvious layered morphology (Fig. S2) and the largest layer spacing, specific surface area and porosity among all samples, as will be discussed shortly in this article.

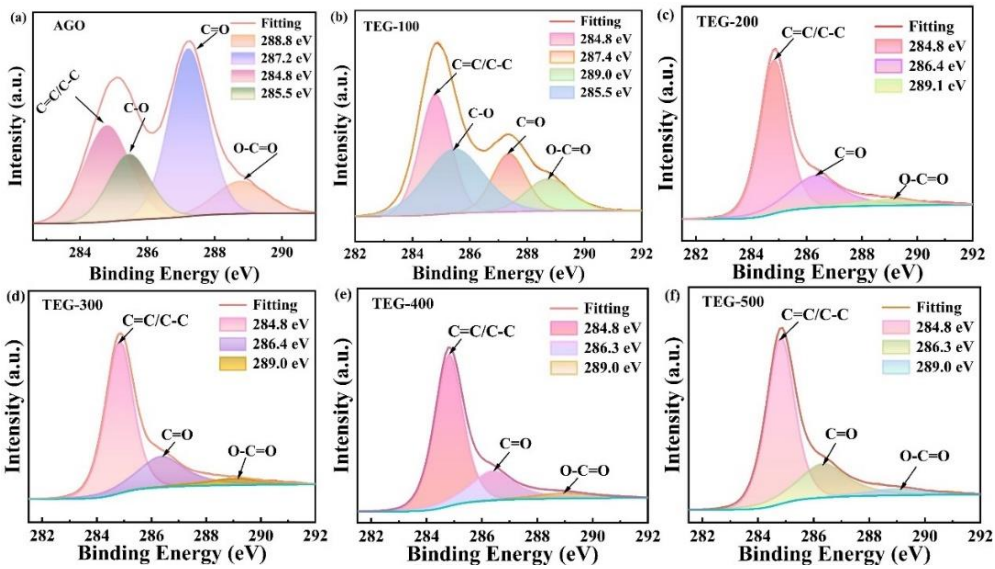

Fig.4. X-ray photoelectron spectrum of (a) C1s of AGO; (b) C1s of TEG-100; (c) C1s of TEG-200; (d) C1s of TEG-300; (e) C1s of TEG-400 and (f) C1s of TEG-500.

According to Fig. 4, the intensities of C 1s peak (284.8 eV) and O 1s peak (532.1 eV) in AGO, TEG-100, and TEG-400 materials indicate a gradual reduction in the abundance of oxygen-containing functional groups. This reduction is further highlighted in the blue boxes in Fig. S5. Table S2 illustrates the amount of oxygen and carbon in samples, according to which the oxygen content in TEG-400 was measured at 5.51 at%. The rise in oxygen content of TEG-500 (6.62 at%) can attributed to the re-stacking of graphene flakes at higher temperatures, as evident according to our microscopic observations. The substantial reduction in oxygen-containing functional groups in TEG-400 increases the increased internal defects, and, consequently, the active sites for Na-ion storage.

According to the AGO spectrum (Fig. 4a), four peaks at 284.8, 285.5, 287.2, and 288.8 eV represent C=C/C-C, C-O, C=O and O-C=O groups, respectively. TEG-100 (Fig. 4b) retains

these functional groups, indicating incomplete reduction and thermochemical exfoliation. Fig. 4c-4f shows that TEG-200 to TEG-500 the C=C/C-C bonds, completely removed C-O, and reduced the amount of C=O and O-C=O.

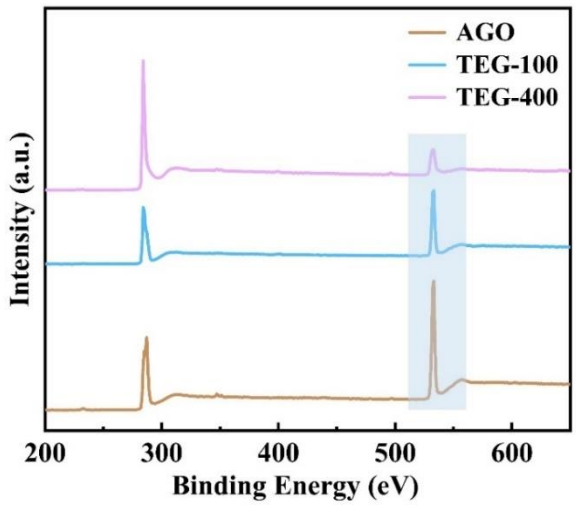

Fig. S5. Full XPS spectra of AGO, TEG-100 and TEG-400.

Table S2. The atomic percentage of carbon and oxygen, based on the XPS C1s and O1s of AGO, TEG-100, TEG-200, TEG-300, TEG-400 and TEG-500.

Sample	C 1s	O 1s
AGO	58.99 %	41.01 %
TEG-100	70.27 %	29.73 %
TEG-200	93.16 %	6.84 %
TEG-300	93.57 %	6.43 %
TEG-400	94.49 %	5.51 %
TEG-500	93.38 %	6.62 %

Table S3 shows the intensity ratio of C=C/C-C:C=O and peak areas (Table S4) in AGO and TEG-X samples. As can be seen, these values reach their maximum in TEG-400, indicating a ratio of 5.084, substantially greater than of AGO (0.575), and also those of TEG-100 (2.062), TEG-200 (4.779), TEG-300 (4.883) and TEG-500 (4.875). This observation exhibits an

enhanced deoxygenation process taking place in TEG-400, increasing its structural defects and providing additional Na-ion storage sites at the electrode/electrolyte interface [56,57]. Notably, the presence of nano-crosslinked porous graphene accelerates the electron transport, resulting in significantly improved electrochemical performance.

Table S3. The intensity ratio of C=C/C-C and C=O functional groups in AGO, TEG-100, TEG-200, TEG-300, TEG-400 and TEG-500.

Materials / Functional group	AGO Peak area	TEG-100 Peak area	TEG-200 Peak area	TEG-300 Peak area	TEG-400 Peak area	TEG-500 Peak area
C1s	C=C/C-C 50716.5	C=C/C-C 57079.5	C=C/C-C 157114.3	C=C/C-C 143608.6	C=C/C-C 167868.2	C=C/C-C 158381.5
	C=O 88245.7	C=O 27679.1	C=O 32875.4	C=O 29411.7	C=O 33020.0	C=O 32489.7
C=C/C-C: C=O	0.575:1	2.062:1	4.779:1	4.883:1	5.084:1	4.875:1

Table S4. The peak area ratio of C=C/C-C and C=O functional groups in AGO, TEG-100, TEG-200, TEG-300, TEG-400 and TEG-500.

Materials / Functional group	AGO Peak area	TEG-100 Peak area	TEG-200 Peak area	TEG-300 Peak area	TEG-400 Peak area	TEG-500 Peak area
C1s	C=C/C-C 86803.1	C=C/C-C 78612.8	C=C/C-C 211381.5	C=C/C-C 187278.6	C=C/C-C 219948.0	C=C/C-C 205576.6
	C=O 130873.8	C=O 41314.7	C=O 84893.0	C=O 63184.7	C=O 64911.1	C=O 70665.8
C=C/C-C: C=O	0.663:1	1.903:1	2.490:1	2.964:1	3.388:1	2.909:1

The thermal stabilities of AGO and TEG-400 were assessed through thermogravimetric analysis (TGA), as depicted in Fig. S6. In the TGA curve of AGO, an initial mass loss below 200 °C is attributed to the desorption of water and other organic molecules present on AGO. A

more significant mass loss occurs between 219°C-274°C, corresponding to the substantial removal of oxygen-containing groups, including C-O, C=O, and O-C=O, aligning with the XPS results. In contrast, TEG-400 exhibits thermal stability, with only minimal mass loss at lower temperatures attributed to the presence of adsorbed water and organic molecules. This observation underscores the fact that TEG-400 lacks substantial oxygen-containing functional groups. The thermal stability of the graphene material, as observed in this study, is noteworthy and aligns with findings in the literature [58].

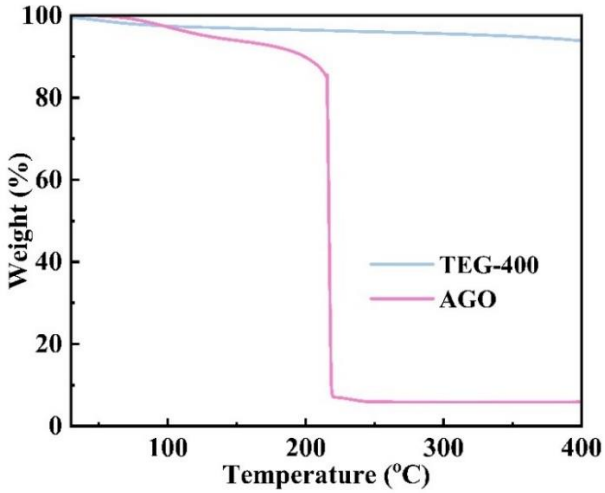

Fig. S6. TGA curve of AGO and TEG-400.

The Brunauer-Emmett-Teller (BET) surface areas of TEG-100, TEG-200, TEG-300, TEG-400, and TEG-500 were measured to be at 135.47, 478.14, 492.78, 517.29, and 502.54 $m^2 \cdot g^{-1}$, respectively (Figs. 5a-e). The considerably lower surface area of TEG-100 is due to its incomplete reduction/exfoliation. In contrast, TEG-400 shows the highest specific surface area due to the efficient exfoliation without occurrence of layer restacking, such as observed in TG-500. As shown in Table S2, we found that the oxygen content of TEG-300 (6.43%) is slightly lower than that of TEG-500 (6,62 at%). Moreover, TEG-500 has a higher value of specific

surface area, but lower porosity in comparison to those of TEG-300. This observation indicates that the temperature and the level of deoxygenation jointly affect the surface characteristics of TEG samples. While TEG-500 experiences an efficient exfoliation at 400 ℃, the partial restacking occurring at higher temperatures slightly reduces its specific surface area in comparison to TEG-400, while still greater than that of TEG-300. Since the thermal treatment was conducted for 2 hours at the target temperature, TEG-500 experienced a considerably shorter period of time at lower temperatures, where efficient deoxygenation could be achieved. Therefore, the rapid restacking of graphene sheets at 500 ºC could lead to trapping of oxygen within TEG-500 before its removal. Based on this, the slightly greater oxygen content of TGE-500 (6.62 at%) in comparison to that of TEG-300 (6.43%) is likely to be explained. The stacked structure and lower porosity in TEG-500 can also explain its inferior electrochemical performance compared to that of both TEG-400 and TEG-300, as elucidated later in this article.

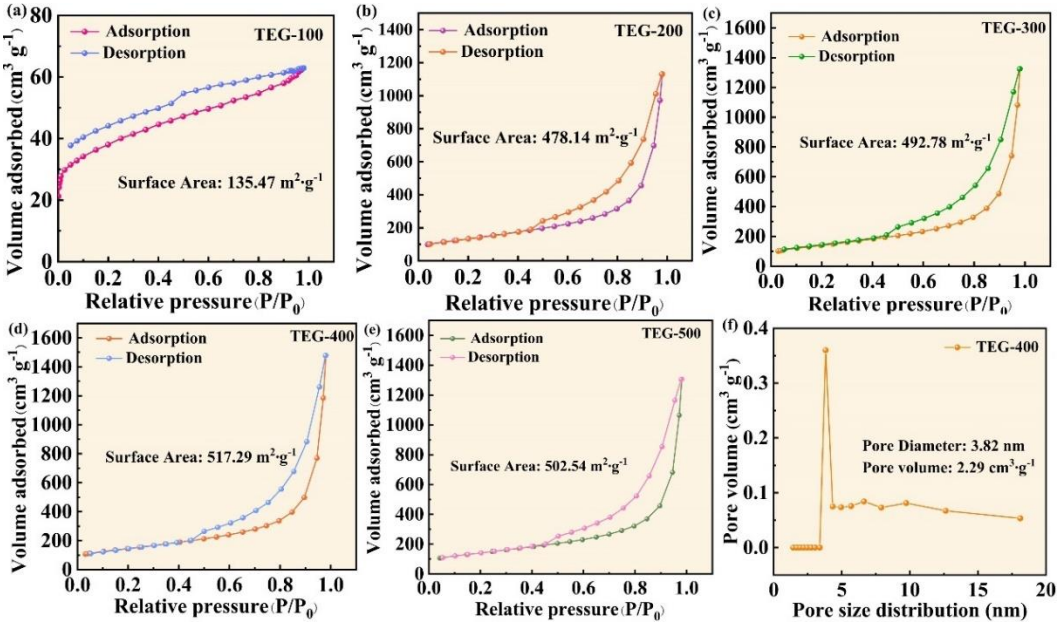

Fig.5. N_2 adsorption/desorption isotherms of (a) TEG-100, (b) TEG-200, (c) TEG-300, (d) TEG-400 and (e) TEG-500. (f) Pore size distribution of TEG-400.

Furthermore, nitrogen adsorption/desorption isotherms and pore size distributions for TEG-X samples are presented in Fig. 5b-f. The isotherms observed reveal a type IV configuration, indicating the presence of porous structure. In the P/P_0 range from 0.5 to 1, the isotherms exhibit an H_3-type hysteresis, indicative of a capillary cohesive structure within the porous material [59]. These findings underscore the highly mesoporous nature of TEG. In addition, Fig. 5f shows the BJH pore size distribution of TEG-400, indicating that the pores are concentrated at ∽3.8 nm with an average size and volume of 3.82 nm and 2.29 $cm^3 \cdot g^{-1}$, respectively. As discussed later in this paper, the improved electrochemical performance of TEG-400 is mainly attributed to the relatively large layer spacing, the prominent contribution of the porous structure, and the large specific surface area of the sample (517.29 $m^2 \cdot g^{-1}$).

Table 2. Surface properties of TEG-X samples, comprising BET specific surface area (S_{BET}), total pore volume (V_T), average pore diameter (d_M), pore volume (V_M) and pore diameter (d_P).

Samples	S_{BET} ($m^2 \cdot g^{-1}$)	V_T ($cm^3 \cdot g^{-1}$)	d_M (nm)	V_M ($cm^3 \cdot g^{-1}$)	d_P (nm)
TEG-100	135.47	0.097	2.87	0.033	3.829
TEG-200	478.14	1.75	14.60	1.809	3.830
TEG-300	492.78	2.05	16.63	2.131	3.841
TEG-400	517.29	2.29	17.69	2.386	3.822
TEG-500	502.54	2.02	16.60	2.093	3.847

Table 2 shows the pore structure parameters for TEG-X samples. As can be observed, the TEG-400 material exhibits the highest specific surface area among all the materials, with a total pore volume and average pore diameter of 2.29 $cm^3 \cdot g^{-1}$ and 17.69 nm, respectively. This suggests that one-step thermochemical exfoliation of AGO effectively removes oxygen-

containing groups in the form of gas species such as water, carbon dioxide, and carbon monoxide. The thermochemical exfoliation process induces the separation of graphene flakes, leading to a reduction in their thickness and an increase in layer spacing. As a result, the specific surface area and pore volume of TEG-400 are significantly augmented through thermochemical exfoliation techniques. The simultaneous presence of a high specific surface area and a mesoporous structure plays key roles in facilitating the charge transfer, thereby enhancing the overall performance of sodium-ion batteries.

3.3. Electrochemical properties of TEG-X samples

To evaluate the sodium-ion storage performance of the TEG-X samples, the prepared material together with binder were coated on copper foil served as current collector; and the electrodes made were assembled into CR2032 coin half-cells. The rate performances of various electrodes from 0.1 to 5 $A \cdot g^{-1}$ are shown in Fig. 6a, from which it can be realized that the nano-crosslinked graphene prepared by the thermochemical exfoliation method at various temperatures exhibit considerably stable Na-ion storage performances. Accordingly, the specific discharge capacities of TEG-100, TEG-200, TEG-300 and TEG-500 were measured to be 182.6, 303.7, 364.2 and 383.0 $mAh \cdot g^{-1}$ after 10 cycles at the current density of 0.1 $A \cdot g^{-1}$, respectively. In contrast, TEG-400 shows the highest specific discharge capacity recorded at 402.4 $mAh \cdot g^{-1}$ under the same condition. This value is more than 10 times higher than that of pure graphite (35 $mAh \cdot g^{-1}$ [60, 61]). Interestingly, after cycling of TEG-400 at various current densities in the range 100-5000 $mA \cdot g^{-1}$, and upon the return to the current density of 100 $mA \cdot g^{-1}$, the material still exhibits a great performance, characterized by the capacity retention of 127.6% (513.7 $mAh \cdot g^{-1}$) after 70 cycles. The uprising the capacity over cycling is attributed to

the activation of the remaining C=O and -COOH functional groups [62, 63] present on the graphene surface. As can be seen in Fig. 6a, TEG-400 shows a capacity of 244.8 $mAh \cdot g^{-1}$ at the current density of 2000 $mA \cdot g^{-1}$ after 50 cycles, and 203.5 $mAh \cdot g^{-1}$ at 5000 $mA \cdot g^{-1}$ after 60 cycles, which are considerably greater than the capacities of TEG-100; 93.7 $mAh \cdot g^{-1}$ at 2000 $mA \cdot g^{-1}$ and 66.6 $mAh \cdot g^{-1}$ at 5000 $mA \cdot g^{-1}$.

As can be observed in Fig. 6a, after 70 Na-ion insertion/extraction cycles, the specific discharge of TEG-400 is significantly higher than those of other samples, which is attributed to the fact the optimum carbon layer spacing in TEG-400 combined with the larger specific surface area of TEG-400 with minimized oxygen-containing groups, improving the electrochemical performance of the sample. In conclusion, nano-crosslinked and porous structured graphene was shown to be beneficial for improving the Na-ion storage performance.

The long-term cycling stabilities of the TEG-X electrodes were tested at the current of 200 $mA \cdot g^{-1}$ as shown in Fig. 6b. All the electrodes exhibit stable performance due to the presence of nano-crosslinked porous graphene structure. In particular, TEG-400 exhibits an initial discharge capacity and coulombic efficiency of 414.1 $mAh \cdot g^{-1}$ and 86%, respectively. The capacity after 300 cycles is still high at 281 $mAh \cdot g^{-1}$; 68% of the initial capacity. Here, we found that temperature has a meaningful impact on the electrochemical performance of the samples, according to which TEG-100 has a lowest specific discharge capacity of 93 $mAh \cdot g^{-1}$ due to incomplete thermochemical exfoliation and reduction. Accordingly, the specific capacity of TEG-400 after 300 cycles is nearly 200 $mAh \cdot g^{-1}$ higher than that of TEG-100. We also observed that the specific capacity of TEG-X samples tends to increase after 50 cycles, although this phenomenon is not evident for TEG-100 and TEG-200. Due to the low heating

temperature, TEG-100 did not undergo the thermochemical exfoliation process, and therefore, its electrochemical performance is unsatisfactory. Thermochemical exfoliation could only be partially achieved in TEG-200 due to insufficient treatment temperature, and consequently, a well-developed pore structure could not be attained in this sample. In TEG-300, TEG-400, and TEG-500, the thermal treatment led to the development of an appropriate pore structure (pore volume > 2 $cm^3 \cdot g^{-1}$) and a large surface area, providing an opportunity for the electrolyte to gradually penetrate into the electrode. This facilitates the contact of sodium ions through the pores with the oxygen-containing groups on the material, thus increasing the specific capacity. According to the literature, the reversible interaction of C=O groups within the porous structure of the electrode with Na^+ can be responsible for the capacity enhancement [64].

The potential-capacity curves of TEG-400 electrode recorded at the 1st, 2nd, 3rd, 4th, 20th, 40th, 60th, 100th, 120th, 160th and 200th cycles are shown in Fig. 6c. Furthermore, the CV curves of the electrode recorded at 0.01-3 V (0.3 $mV \cdot s^{-1}$) during the first four consecutive cycles are shown in Fig. 6d. Shown in Fig. 6c, the electrode underwent activation at the first three cycles under the current density of 30 $mA \cdot g^{-1}$, experiencing discharge capacities of 583.7, 459.3 and 468.4 $mAh \cdot g^{-1}$, respectively. It's worth noting that the discharge specific capacities of 414.1 $mAh \cdot g^{-1}$ (4th cycle), 401.6 $mAh \cdot g^{-1}$ (20th cycle), 525.0 $mAh \cdot g^{-1}$ (40th cycle) and 480.0 $mAh \cdot g^{-1}$ (60th cycle) were measured at the enhanced current density of 200 $mA \cdot g^{-1}$. As discussed, the capacity increase observed between the 4th and 20th cycles is due to the presence of the nano-crosslinked porous structure that promotes the gradual interaction between sodium ions and the surface oxygen-containing groups, increasing the capacity over cycling. As the oxygen functional groups on graphene are consumed, graphene itself continues to provide

specific capacity. In subsequent cycles of 100, 120, 140, 160 and 200 cycles the capacity fading becomes relatively smaller. The GCD curve shows that the discharge specific capacity at the 100th cycle is 400.1 $mAh \cdot g^{-1}$, and the specific capacity retention rates at the subsequent 120th, 140th, 160th and 200th discharges are 96.9, 95.9, 94.6 and 90.7% respectively.

As shown in Fig. 6d, the CV curves of the TEG-400 material measured at 0.3 $mV \cdot s^{-1}$ show a pair of redox peaks below about 0.2 V, which can correspond to the insertion/extraction of Na^+ into graphene material [27]. In the first scan, the reduction peak starting at about 0.70 V with the peak at 0.43 V is related to the formation of solid electrolyte interphase (SEI) film on the electrode formed due to the decomposition of electrolyte, with the oxidation peak appears at about 0.8 V [27,65]. It is obvious that the CV curves of second and forth cycles overlap well, which means that the Na^+ insertion/extraction into/out of the TEG-400 electrode is highly reversible.

As exhibited in Fig. 6e, the electrochemical performance of TEG-400 is highly stable, with a specific capacity of 219.9 $mAh \cdot g^{-1}$ recorded after 1000 cycles at the current density of 2000 $mA \cdot g^{-1}$. This performance stability is attributed to the nano-cross-linked structure of graphene constructing a super-porous structure with the pore size of 3.82 nm and the interlayer spacing of 0.362 nm, providing interconnected channels for charge transportation, and abundant active sites for the reversible accommodation of sodium ions, with a radius of 0.102 nm [61]. The electrochemical characterizations mentioned above confirm that TEG-X nanostructured materials exhibit excellent tunable multiplicity, good cycling stability, and high specific capacity. These characteristics are attributed to the unique morphological and structural features of TEG-X, which enhance the capacity and rate performance of the resulting electrodes.

Table S5. Parameters associated with the electrical conductivity of AGO and TEG-400.

Samples	Resistance value (Ω)	Cross-sectional area (m^2)	Thickness (m)	Volumetric resistivity (Ω, m)	Conductivity ($S \cdot m^{-1}$)
AGO	7.05E+04	7.85E-05	3.98E-03	1.39E+03	7.19E-04
TEG-400	6.16E-02	7.85E-05	4.50E-04	1.07E-02	9.30E+01

In graphene nano-crosslinking, the thin-layer and mesoporous graphene structure enables ions to pass directly and quickly instead of bypassing the graphene; thus, significantly shortening the charge transfer diffusion distance. To further explore the charge transfer preparties of TEG-X electrodes, electrochemical impedance spectroscopy was performed. According to the typical Nyquist plot of the sample (Fig. 6f), the impedance spectra consist of a semicircular arc in the high-frequency region and a straight line in the mid- to low-frequency region, with the corresponding equivalent circuit model presented as inset in Fig. 6f. The semicircle diameter in the high-frequency region corresponds to the charge transfer resistance (R_{ct}) at the interface between the electrode and the electrolyte. The R_{ct} values of TEG-X can be measured to be 36.75, 11.67, 12.82, 8.04 and 17.41 Ω for X=100, 200, 300, 400 and 500, respectively. Notably, TEG-400 shows the lowest R_{ct} value, indicating the enhanced charge transfer in this sample. In addition, the lines in the mid-low frequency region of EIS spectra, corresponding to the Warburg diffusion behavior, show a relatively deep slope, indicating high values of ion diffusion rate within the electrode material [66]. Therefore, the unique structure of TEG-400 can significantly improve the intercalation/deintercalation kinetics of sodium ions.

We further measured the electrical conductivity of the samples using a high precision resistance tester using Eqs. (1) and (2), and the calculated data are shown in Table S5. As can be seen, the conductivities of the AGO and TEG-400 are 7.19×10^{-4} and 93 $S \cdot m^{-1}$, respectively,

providing the evidence that TEG-400 is ≈10^5 times more conductive than the AGO.

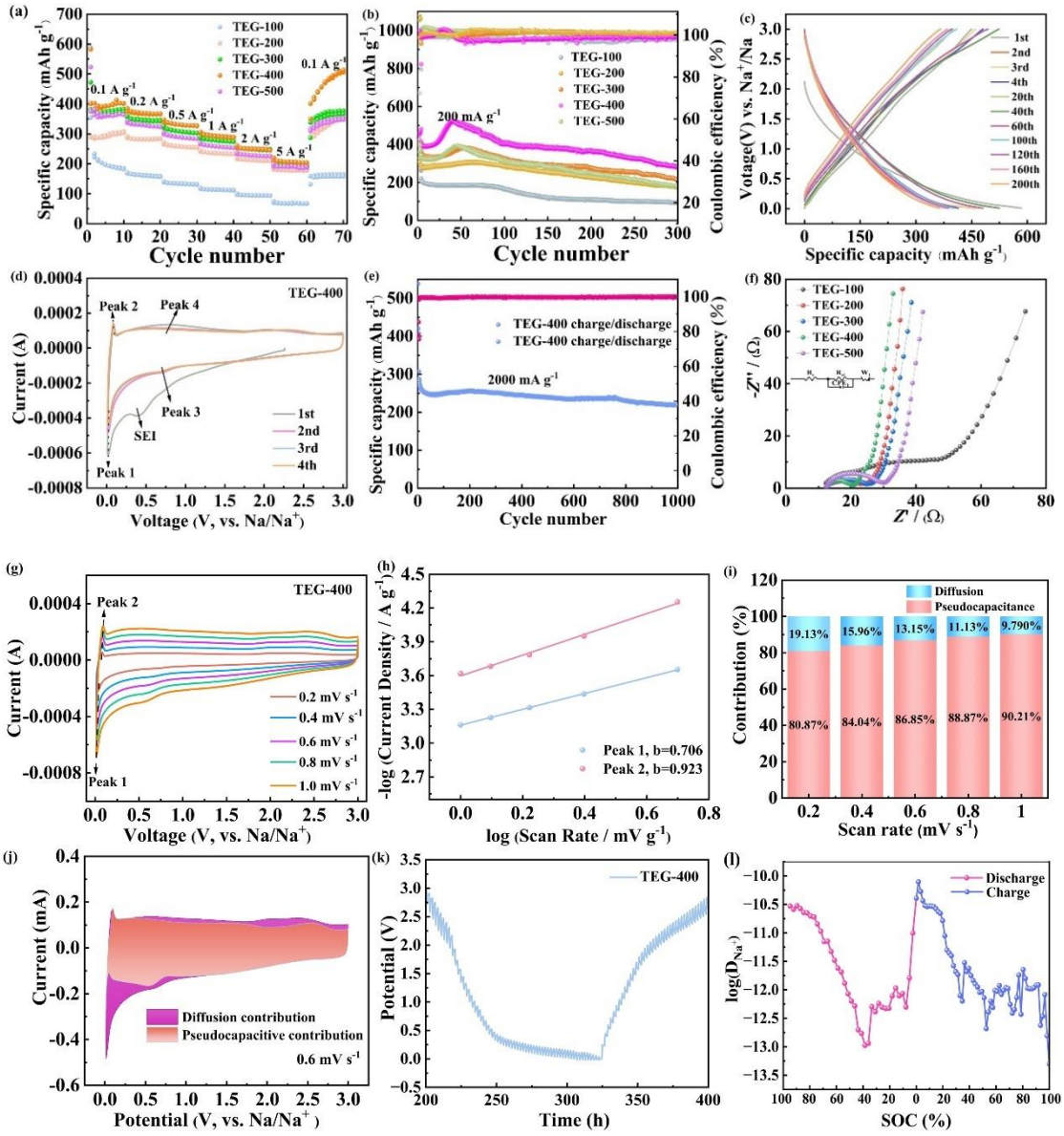

Fig. 6. (a) Na^+ storage rate performances, and (b) cycling performances of TEG-X samples. (c) GCD curves of TEG-400 electrode at 200 mA·g^{-1}. (d) CV curves of TEG-400 at 0.3 mV·s^{-1}. (e) Prolonged cycling performance of TEG-400 at 2000 mA g^{-1}. (f) Nyquist plots of TEG-X electrodes. (g) CV curves of TEG-400 at different scan rates. (h) b values obtained for the peaks shown in(g) based on the linear fitting. (i) Contribution ratios of the pseudocapacitance and diffusion-based capacities at various scan rats. (j) CV curve of TEG-400 and the calculated pseudocapacitive contribution shown as the shaded region at a scan rate of 0.6 mV·s^{-1}. (k) The GITT curves of TEG-400 anode. (l) The calculated Na-ion diffusion coefficients of TEG-400 electrode during the sodiation and desodiation cycles.

It should be noted that the electrical conductivity of TEG-400 is lower than that of

alternative graphene materials, such as that reported in our previous work [67]. The relatively diminished conductivity of TEG-400 can be attributed to the introduction of defects, as discussed earlier in this article. According to the literature [61], when the Raman I_D/I_G is lower than 0.4, the incorporation of sodium ions into carbon materials faces significant challenges. Conversely, when the I_D/I_G exceeds 1.2, the conductivity becomes too low to achieve effective electrochemical performance [61]. Hence, the electrical conductivity alone is not the sole determinant of the electrochemical performance of graphene materials. The remarkable performance of TEG-400 in this study can be ascribed to a delicate balance between electrical conductivity and defect levels. This balance results in reduced charge transfer resistance, facilitated by the nano-crosslinked structure, large pore volume, and excellent specific surface area of the electrode.

3.4. Electrokinetic characterization

The CV curves of the TEG-400 electrode, recorded at various scan rates ranging from 0.2 to 1.0 $mV \cdot s^{-1}$, are depicted in Fig. 6g. The Na^+ storage mechanism can be categorized into diffusion-controlled and pseudocapacitive-controlled charge storage. This distinction can be made using the power-type law equation presented below [68, 69]:

$$i = av^b \quad (5)$$

Here, i represents the current, v is the sweep rate, and a and b are adjustable constants. The value of b can be determined from the slope of log (i) versus log (v), as illustrated in Fig. 6h. The calculated b values for the cathode and anode peaks in Fig. 6g are 0.706 and 0.923, respectively. A b value of 0.5 indicates a diffusion-controlled process, while 1.0 indicates a

capacitance-controlled process [70]. The b value associated with the cathodic peak fall within the range of 0.5 to 1.0, suggesting a mixed mechanism involving capacitance and diffusion control effects in the charge storage process. Conversely, the anodic peaks exhibit a b value close to 1.0, indicating pseudocapacitive control. The pseudocapacitive contribution to the sodium-ion storage performance of the electrode can be analyzed using following equation [68-70]:

$$i\,(V) = k_1 v + k_2 v^{1/2} \quad (6)$$

where $k_1\nu$ and $k_2\nu^{1/2}$ represent the pseudocapacitive contribution and diffusive contributions. Fig. 6i shows the contributions of capacitive and diffusive charge transfer at different scan rates. It is clear that the pseudocapacitive contribution increases with the scan rate and dominates the total specific capacity. As shown in Fig. 6j, the capacitive contribution (shaded area) accounts for 86.85% of the total current at a scan rate of 0.6 $mV \cdot s^{-1}$. The fast charge transfer rate in the TEG-400 electrode can be related to the unique microstructure of the sample as discussed earlier.

Sun et al. [71] reported that carbon materials with d-spacing of 0.36-0.40 nm typically contains semi-ordered microcrystals, regarded as "pseudo-graphitized" carbons. Such carbon materials may present a satisfactory Na-ion storage performance. The Na-ion storage in such carbon material can be corresponded to the sloped or plateau region of a typical GCD curves of the sample, summarized into three categories: (1) Na^+ ions embedded into the graphitic layers; (2) Na^+ ions filled within nanopores of the flakes; and (3) Na^+ ions adsorbed at the surface defect sites on the surface [72-78]. Based on these three sodium storage behaviors.

Based on these characteristics, the mechanism of action for the excellent electrochemical performance is proposed in this study to be both intercalation and adsorption. The sodium ion storage behavior observed in this study mainly involves the adsorption of Na ions at surface defect sites. The outstanding electrochemical performance of TEG-400 is predominately attributed to the high density of defects, substantial pore volume, and extensive specific surface area of its nano-crosslinked porous structure. Furthermore, the increased interlayer spacing of TEG-400, as indicated by XRD analysis, enhances pseudo-capacitive Na-ion storage, thereby enhancing the overall electrochemical properties of the material. These features contribute to improved wettability of the carbon material to sodium ions, providing a greater number of electrochemically active sites. Additionally, the prevailing pseudocapacitive control behavior results in rapid kinetic properties, thereby enhancing the rate capability and cycling performance of the electrode materials.

The diffusion coefficients of Na^+ into and out of the electrodes (D_{Na^+}) were evaluated by the electrostatic intermittent titration technique (GITT). GITT curves for the second cycle of TEG-400 recorded at room temperature at a current of 30 $mA \cdot g^{-1}$ and a pulse/relaxation time of 30 min/1.5 h are shown in Fig. 6k and Fig. 6l. These data were used to calculate D_{Na^+} values at different voltages according to Equation (7) [79]:

$$D = \frac{4}{\pi\tau}\left(\frac{n_m V_m}{S}\right)^2 \left(\frac{\Delta E_s}{\Delta E_t}\right)^2 \quad (7)$$

Here, n_m represents the molar value of TEG-400, τ and V_m denote the relaxation time (s) and molar volume of TEG-400 ($cm^3 \cdot mol^{-1}$), respectively. S represents the contact area between the active material and the electrolyte (cm^3), ΔE_s indicates the steady-state potential change during the current pulse, and ΔE_t represents the potential

change in a current pulse after subtracting the IR drop. The GITT experiment was employed to investigate the sodium-ion diffusion coefficient of nano-crosslinked porous graphene, and Fig. 6k shows the corresponding data obtained from the GITT analysis according to Eq. (7) during the discharge/charge process. The sodium-ion diffusion coefficient (D_{Na+}) of TEG-400 was determined to fall within the range of 10^{-13} to 10^{-10} $cm^2 \cdot s^{-1}$ during the sodiation and desodiation events (Fig. 6l). This calculated value can be compared with those reported for other anode materials; for instance, D_{Na+} values for commercial hard carbon with nano-zeolite and carbon black additive (averaging 1×10^{-12} $cm^2 \cdot s^{-1}$) [80], platanus-derived porous hard carbon (averaging 1×10^{-16} $cm^2 \cdot s^{-1}$) [81], and N, S co-doped carbon (averaging 1.5×10^{-15} $cm^2 \cdot s^{-1}$) [82]. The rapid sodium diffusion behavior of nano-crosslinked porous carbon in TEG-400 was further confirmed by its significantly larger D_{Na}^{+} value.

Displayed in Fig. S7, the Na-ion storage performance of TEG-400 can be compared to other materials documented in the literature [28, 71, 83-89], considering current density, number of cycles, and specific capacity. The data depicted in Fig. S7 has been organized into Table S6. Notably, the nano-crosslinked porous TEG-400 occupies a distinguished position among alternative electrode materials. The sample was prepared using a straightforward thermo-chemical exfoliation method, offering economic advantages in contrast to alternative approaches such as hydrazine reduction [28], high-temperature calcination [85], surface-induced capacitive process (SCP) [87], and surface modification [88].

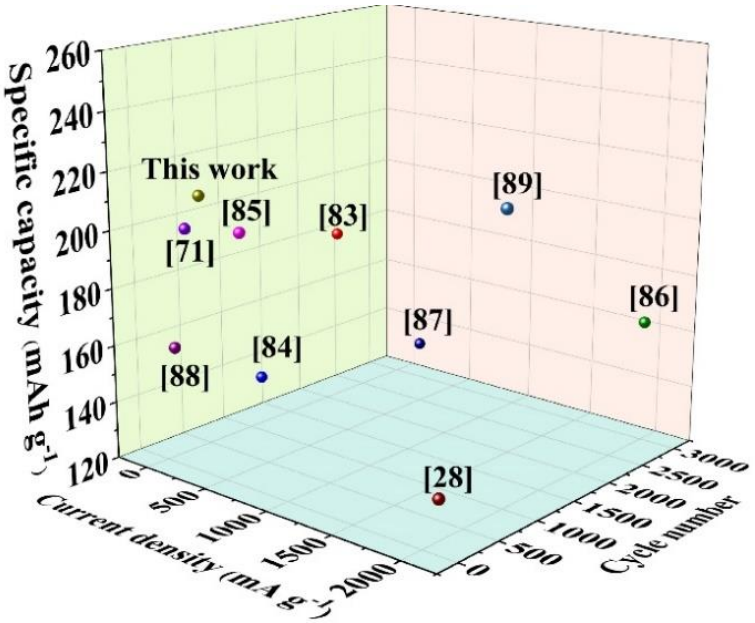

Fig. S7. Na-ion storage Performance TEG-400 in comparison to alternative materials reported in the literatures.

Table S6. Summary of the data presented in Fig. S7

Samples	Method	Current density $mA \cdot g^{-1}$	Cycle number	Specific capacity $mAh \cdot g^{-1}$
Expanded graphite [83]	Sonication	100	2000	184
Reduced graphene oxide [84]	Annealed (900°C)	100	1000	140
Carbon nanosheet frameworks [85]	High temperature calcination (1100°C)	500	210	203
Holey RGO [86]	H_2O_2 treatment/ annealed	2000	3000	163
Layered graphene [87]	SCP design	500	2500	142
Hard Carbons [71]	Pyrolysis (800°C)	50	200	200
AB-PRGO [88]	Chemical method	50	50	160
Double-carbon composites [28]	Situ hydrothermal synthesis	2000	200	134
Porous graphdiyne [89]	Chemical synthesis	100	300	211
This work	Thermochemical exfoliation	2000	1000	219

3.5. Na-ion storage performance

To further elucidate the enhanced electrochemical performance of the TEG-400 electrode,

we conducted electron microscopy studies. Figs. 7a and b display the scanning electron microscopy (SEM) micrographs of the TEG-400 electrode, captured before cycling and after 100 cycles under fully discharged conditions, cycled at a current density of 200 $mA \cdot g^{-1}$. The micrographs confirm the electrode's remarkable mechanical stability throughout the cycling process. According to Fig. 7b, the presence of uniformly distributed microcracks is apparent; however, the electrode remains structurally integrated. This integrity is further confirmed in Figs. 7c and 7d, where SEM micrographs are taken from the cross-section of the sample before cycling and after 100 cycles at fully discharged conditions, respectively. Notably, the thickness of the electrode measures around 22 μm before cycling and approximately 26 μm after 100 cycles, indicating a modest increase of 4 μm. This observation underscores the electrode's capability to maintain its structural integrity over the course of cycling.

It is noteworthy to mention that graphene-based materials utilized in batteries, as reported in the literature, often experience significant volume expansion during cycling [90-92]. This expansion can lead to a rapid degradation of the electrochemical properties of the electrode materials. In contrast, the TEG-400 electrode does not suffer from the issue of secondary volume exfoliation, resulting in outstanding and sustained electrochemical performance.

Figs. 7e-i show TEM micrographs of the electrode after 100 cycles at fully discharged condition. The low-magnification TEM micrograph depicted in Fig. 7e reveals the uniform embedding of sodium species into the nano-crosslinked structure of the graphene material. As observed in the high-resolution TEM (HRTEM) micrograph of Fig. 7f, the presence of crystalline nanoparticles, approximately 5 nm in size, on the graphene material becomes apparent. Fast Fourier transform (FFT) patterns recorded on two nanoparticles, as illustrated in

Fig. 7f, are presented in Figs. 7g and h. Accordingly, the lattice spacings of 0.19 nm and 0.17 nm could be attributed to the (121) and (002) crystalline planes of Na_2O, respectively. Also, the lattice spacings of 0.21 nm could be attributed to the (200) crystalline planes of Na [93, 94]. The FFT pattern recorded on the entire area of Fig. 7f is shown in Fig. 7g-i. The pattern reveals the existence of spots and rings. In addition to the spots corresponding to Na_2O and Na, the ring exhibiting an interlayer spacing of 0.36 nm represents the (002) planes of graphitic carbon, confirming the presence of graphene material.

The nano-network crosslinked porous structure in TEG-400 (Fig. 2) provides the largest layer spacing and the smallest sheet thickness (Table 1), as well as the highest surface and porosity (Table 2) among all samples. These features promote the Na-ion storage performance of the material, based on the following points. First, the oxygen-containing functional groups on the sample, and particularly -C=O and -COOH [95-97] provide favorable sites adsorption and reversible redox interactions of Na ions. Jia et al. [98] indicated the redox reaction between carbonyl groups and Na ($-C=O + Na^+ + e^- \rightarrow -C-O-Na$) contributes to the enhanced Na^+ storage capacity in oxygen-doped carbon anode. Our results demonstrate that porosity plays a crucial role in the efficient utilization of such adsorption sites. When the porosity is lower than 2 $m^3 \cdot g^{-1}$, the contact between the electrolyte and oxygen-containing groups is limited. In these samples, TEG-100 and TEG-200 do not have obvious upward trend in discharge specific capacity can be seen (Fig. 6b). Secondly, the increased interlayer spacing of graphene materials can promote sodium ion intercalation. In this case, the gradual penetration of electrolyte into the porosity of carbon can promote such surface intercalation phenomena, increasing the capacity of samples, as shown in TEG-400. However, during the cycling process, volume changes caused by the

insertion and extraction of Na-ions gradually close up the micropores, leading to microstructural collapse and decreasing the capacity of the material over prolonged cycling, as can be observed in Fig. 6b.

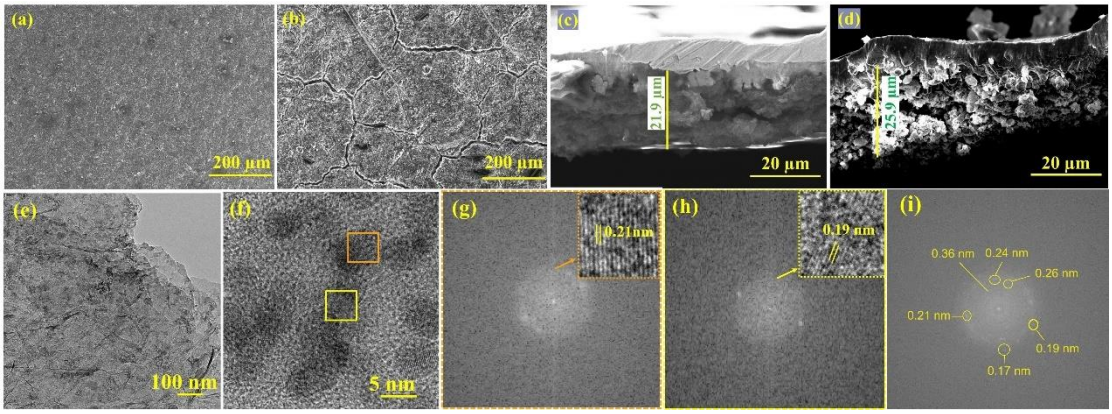

Fig. 7. SEM micrographs of (a) TEG-400 electrode before cycling. (b) TEG-400 electrode after 100 cycles at fully discharged condition. (c) Cross-sectional of TEG-400 electrode before cycling; and (d) after 100 sodium-ion insertion/extraction cycles at discharged condition. (e) Low- and (f) high-magnification TEM micrographs of TEG-400 electrode after 100 cycles at discharged condition. (g) and (h) FFT patterns recorded in the crystals shown in (f). (i) FFT pattern recorded on the whole area of (f).

Figs. S8 shows the TEM micrograph TEG-400 after 100 cycles at fully charged condition. As can be seen, the semi-amorphous nature of the graphene material can be clearly observed (Fig. S8b), while the presence of crystalline nanoparticles is less observable in comparison with that of discharged sample (Fig. 7). It signifies the remarkably reversible accommodation of sodium within the graphite material, resulting in the restoration of its original structure after the depolarization process [99]. This observation aligns with the electron diffraction pattern of the discharged sample (Fig. S8c), where only rings associated with the graphene material are evident. Future research should explore the full-cell performance of TEG-X samples and the influences of other parameters such as the electrolyte composition and temperature.

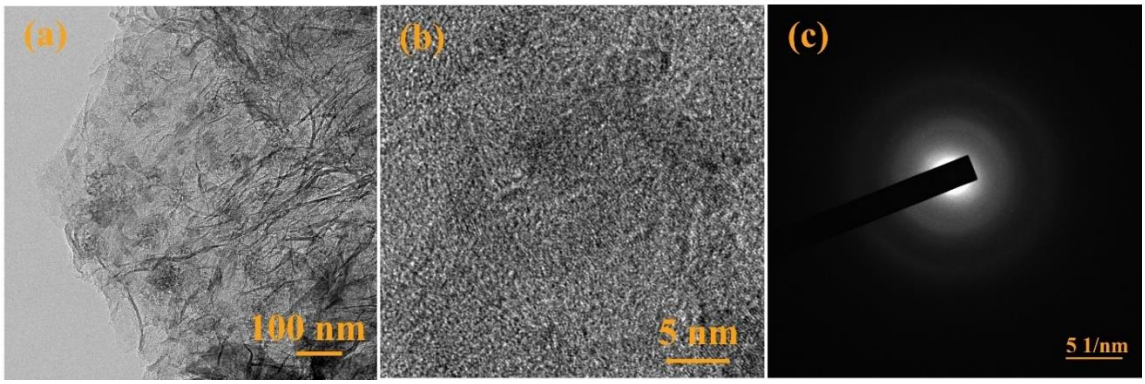

Fig.S8. (a) Lower, and (b) higher magnification TEM micrographs of cycled TEG-400 electrode at full charged status after 100 cycles at 2000 mA·g^{-1}. (c) Diffraction pattern of the electrode sheet after TEG-400 cycling.

4 Conclusion

In conclusion, this study focuses on the preparation and Na-ion storage performance of thermally-exfoliated graphene (TEG) materials. A novel, cost-effective, and precisely controlled thermochemical exfoliation method was introduced for the synthesis of high-quality nano-crosslinked graphene. This method utilizes acidic graphene oxide, containing a substantial amount of oxygen functional groups, as the precursor material. The subsequent controlled thermal treatment leads to the removal of these groups, introducing structural defects, a large pore volume, and surface area, while forming a nano-crosslinked structure. The TEG-400 sample, thermally treated at 400 °C, exhibited a mesoporous structure with a specific surface area of 517.3 $m^2 \cdot g^{-1}$, pore volume of 2.3 $cm^3 \cdot g^{-1}$, and a pore size of 3.82 nm. In this sample, a controlled introduction of defects involves the removal of oxygen-containing functional groups, resulting in the formation of graphene material with a carbon hybridization sp^2/sp^3 ratio of 2.45, providing a balance between the level of defects, porosity structure and the electrical conductivity of the sample. This material demonstrated an enhanced rate performance, revealing a notable specific capacity of 402.4 mAh·g^{-1} at 100 mA·g^{-1} after 10

cycles, 244.8 mAh·g^{-1} after 50 cycles at 2000 mA·g^{-1}, and 203.5 mAh·g^{-1} after 60 cycles at 5000 mA·g^{-1}, coupled with an outstanding capacity of 513.7 mAh·g^{-1} after 70 cycles upon reverting to the current density of 100 mA·g^{-1}. Moreover, TEG-400 exhibited a high initial coulombic efficiency of 86% at 200 mA·g^{-1}, with an exceptional specific capacity of 281 mAh g^{-1} even after 300 cycles (200 mA·g^{-1}), and a capacity of 219 mAh·g^{-1} after 1000 cycles at a high current density of 2000 mA·g^{-1}, outperforming alternative TEG samples fabricated at different temperatures. This work unequivocally establishes that graphene nanomaterials with nano-crosslinked mesoporous structures hold promise as anode materials for the development of high-performance sodium-ion batteries and other energy devices.

Declaration of Competing Interest

The authors declare that they have no known competing financial interests or personal relationships that could have appeared to influence the work reported in this paper.

Acknowledgment

This work was supported by the National Natural Science Foundation of China (51671052, 51750110513 and 52250610222), the Fundamental Research Funds for the Central Universities (N182502042, N2025001) and the Liao Ning Revitalization Talents Program (XLYC1902105).

References

[1] K.J. Griffith, K.M. Wiaderek, G. Cibin, L.E. Marbella, C.P. Grey, Niobium tungsten oxides for high-rate lithium-ion energy storage, Nature, 559 (2018) 556-563, https://doi.org/10.1038/s41586-018-0347-0

[2] B. Wang, T.T. Ruan, Y. Chen, F. Jin, L. Peng, Y. Zhou, D.L. Wang, S.X. Dou. Graphene

based composites for electrochemical energy storage, Energy Stor. Mater., 24(2020)22-51. https://doi.org/10.1016/j.ensm.2019.08.004

[3] W. Luo, F. Shen, C. Bommier, H. Zhu, X. Ji, L. Hu, Na-ion battery anodes: materials and electrochemistry, Acc. Chem. Res., 49 (2016) 2569-2581, https://doi.org/10.1021/acs.accounts.5b00482

[4] C. Yang, J. Chen, X. Ji, T.P. Pollard, X. Lu, C.J. Sun, S. Hou, Q. Liu, C. Liu, T. Qing, Y. Wang, O. Borodin, Y. Ren, K. Xu, C. Wang, Aqueous Li-Ion Battery Enabled by Halogen Conversion-Intercalation Chemistry in Graphite, Nature, 569 (2019) 245-250, https://doi.org/10.1038/s41586-019-1175-6

[5] C. Zhao, Q. Wang, Z. Yao, J. Wang, B. Sánchez-Lengeling, F. Ding, X. Qi, Y. Lu, X. Bai, B. Li, H. Li, A. Aspuru-Guzik, X. Huang, C. Delmas, M. Wagemaker, L. Chen, Y. Hu, Rational design of layered oxide materials for sodium-ion batteries, Science, 370 (2020) 708-711, https://doi.org/10.1126/science.aay9972

[6] Y. Li, Y. Lu, C. Zhao, Y. S. Hu, M.M. Titirici, H. Li, X. Huang, L. Chen, Recent advances of electrode materials for low-cost sodium-ion batteries towards practical application for grid energy storage, Energy Stor. Mater., 7 (2017) 130-151, https://doi.org/10.1016/j.ensm.2017.01.002

[7] H. Xue, Q. Sun, R. Lu, C. Liu, Electrochemical characterization of graphene-type materials obtained by electrochemical exfoliation of graphite, J. Electroanal. Chem., 902 (2021) 115084, https://doi.org/10.1016/j.jelechem.2021.115809

[8] H. Pan, Y.S. Hu, L. Chen, Room-temperature stationary sodium-ion batteries for large-scale electric energy storage, Energy Environ. Sci., 6 (2013) 2338-2360, https://doi.org/10.1039/c3ee40847g

[9] S. Li, K. Wang, G. Zhang, S. Li, Y. Xu, X. Zhang, X. Zhang, S. Zheng, X. Sun, Y. Ma, Fast Charging Anode Materials for Lithium-Ion Batteries: Current Status and Perspectives, Adv. Funct. Mater., 32 (2022) 2200796, https://doi.org/10.1002/ADFM.202200796

[10] R.C. Asher, S.A. Wilson, Lamellar compound of sodium with graphite, J. Inorg.& Nuclear Chem., 181 (1958) 113-123, https://doi.org/10.1016/0022-1902(59)80118-4

[11] Y.J. Fang, D.Y. Luan, X.W. Lou, Recent advances on mixed metal sulfides for advanced sodium-ion batteries, Adv. Mater., 32 (2020) 2002976,

https://doi.org/10.1002/adma.202002976

[12] V. Palomares, M. Casas-Cabanas, E. Castillo-Martínez, M.H. Han, T. Rojo, Update on Na-based battery materials, A growing research path, Energy Environ. Sci., 6 (2013) 2312-2337, https://doi.org/10.1039/c3ee41031e

[13] H. He, D. Huang, W. Pang, D. Sun, Q. Wang, Y. Tang, X. Ji, Z. Guo, H. Wang, Plasma-Induced Amorphous Shell and Deep Cation-Site S Doping Endow TiO2 with Extraordinary Sodium Storage Performance, Adv. Mater., 30 (2018)1801013, https://doi.org/10.1002/adma.201801013

[14] H. Zhao, A. Rezaei, A.R. Kamali, Electrolytic conversion of natural graphite into carbon nanostructures with enhanced electrical conductivity and Na-ion storage performance, J. Electrochem. Soc., 169 (2022) 054512, https://doi.org/10.1149/1945-7111/ac6bc2

[15] Y.J. Kang, S.C. Jung, J.W. Choi, Y.K. Han, Important Role of Functional Groups for Sodium Ion Intercalation in Expanded Graphite, Chem. Mater., 27 (2015) 5402-5406, https://doi.org/10.1021/acs.chemmater.5b02024

[16] K. Wang, Y.B. Xu, Y. Li, V. Dravid, J.S. Wu, Y. Huang, Sodium storage in hard carbon with curved graphene platelets as the basic structural units, J. Mater. Chem. A, 7 (2019) 3327-3335, https://doi.org/10.1039/C8TA11510A

[17] Z.L. Jian, C. Bomrnier, L.L. Luo, Z.F. Li, W.T. Wang, C.M. Wang, P.A. Greaney, X.L. Ji, Insights on the Mechanism of Na-Ion Storage in Soft Carbon Anode, Chem. Mater., 29 (2017) 2314-2320, https://doi.org/10.1021/acs.chemmater.6b05474

[18] X. Xie, K. Kretschmer, J. Zhang, S. Bing, D. Su, G. Wang, Sn@CNT nanopillars grown perpendicularly on carbon paper: A novel free-standing anode for sodium ion batteries, Nano Energy, 13 (2015) 208-217, https://doi.org/10.1016/j.nanoen.2015.02.022

[19] L. Zhu, Z. Zhu, J. Zhou, Y. Qian, Kirkendall effect modulated hollow red phosphorus nanospheres for high performance sodium-ion battery anodes, Chem. Commun., 56 (2020) 11795-11798, https://doi.org/10.1039/d0cc05087c

[20] S. Zhang, Y. Li, M. Li, Porous Hard Carbon Derived from Walnut Shell as an Anode Material for Sodium-Ion Batteries, JOM, 8 (2018) 2030-2042. https://doi.org/10.1007/s11837-018-2789-0

[21] M.F. El-Kady, Y.L. Shao, R.B. Kaner, Graphene for batteries, supercapacitors and beyond,

Nat. Rev. Mater., 1(2016) 16033, https://doi.org/10.1038/natrevmats.2016.33

[22] Y.D. Zhu, Y. Huang, C. Chen, M.Y. Wang, P.B. Liu, Phosphorus-doped porous biomass carbon with ultra-stable performance in sodium storage and lithium storage, Electrochim. Acta, 321 (2019) 134698, https://doi.org/10.1016/j.electacta.2019.134698

[23] J.X. Song, Z.X. Yu, M. Gordin, S. Hu, R. Yi, D.H. Tang, T. Walter, M. Regula, D.W. Choi, X.L. Lin, A. Manivannan, D.H. Wang, Chemically Bonded Phosphorus/Graphene Hybrid as a High-Performance Anode for Sodium-Ion Batteries, Nano Lett., 14 (2014) 6329-6335, https://doi.org/10.1021/nl502759z

[24] Y.J. Yang, D.M. Tang, C. Zhang, Y.H. Zhang, Q.F. Liang, S.M. Chen, Q.H. Weng, M. Zhou, Y.M. Xue, J.W. Liu, J.H. Wu, Q.H. Cui, C. Lian, G.L. Hou, F.L. Yuan, Y. Bando, D. Golberg, X. Wang, “Protrusions” or “holes” in graphene: which is the better choice for sodiumion storage, Energy Environ. Sci., 10 (2017) 979-986, https://doi.org/ 10.1039/c7ee00329c

[25] H. Kim, G. Yoon, K. Lim, K. Kang, A comparative study of graphite electrodes using the co-intercalation phenomenon for rechargeable Li, Na and K batteries, Chem. Commun., 52 (2016) 12618-12621, https://doi.org/10.1039.C6CC05362A

[26] K.S. Novoselov, A.K. Geim, S.V. Morozov, D. Jiang, Y. Zhang, S.V. Dubonos, V. Grigorieva, A.A. Firsov, Electric field effect in atomically thin carbon films, Science, 306 (2004) 666-669, https://doi.org/10.1126/science.1102896

[27] Y. Tong, Y.J. Wu, Z.H. Liu, Y.S. Yin, Y.J. Sun, H.Y. Li, Fabricating multi-porous carbon anode with remarkable initial coulombic efficiency and enhanced rate capability for sodium-ion batteries, Chin. Chem. Lett., 34 (2023) 107443, https://doi.org/10.1016/j.cclet.2022.04.041

[28] N. Wen, S.Y. Chen, J.J. Feng, K. Zhang, Z.Y. Zhou, X.L. Li, Q.H. Fan, Q. Kuang, Y.Z. Dong, Y.M. Zhao, In situ hydrothermal synthesis of double-carbon enhanced novel cobalt germanium hydroxide composites as promising anode material for sodium ion batteries, Dalton Trans., 50 (2021) 4288-4299, https://doi.org/10.1039/D1DT00135C

[29] N.F. Zhou, G. Luo, W. Qin, C. Wu, C.K. Jia, One-pot synthesis of boron-doped cobalt oxide nanorod coupled with reduced graphene oxide for sodium ion batteries, J. Colloid Interface Sci., 640 (2023) 710-718, https://doi.org/10.1016/j.jcis.2023.03.028

[30] S. Chae, T. Lee, W. Kwon, H. Kang, H.J. Seo, E. Kim, E. Jeong, J.H. Lee, S.G. Lee, Longitudinally grown pyrolyzed quinacridones for sodium-ion battery anode, Chem. Eng. J., 453 (2023) 139805, https://doi.org/10.1016/j.cej.2022.139805

[31] K. Krishnamoorthy, M. Veerapandian, K. Yun, S.J. Kim, The Chemical and structural analysis of graphene oxide with different degrees of oxidation, Carbon, 53(2013)38-49, https://doi.org/10.1016/j.carbon.2012.10.013

[32] M. Cabello, X. Bai, T. Chyrka, G.F. Ortiz, P. Lavela, R. Alcantara, J.L. Tirado, On the Reliability of Sodium Co-Intercalation in Expanded Graphite Prepared by Different Methods as Anodes for Sodium-Ion Batteries, J. Electrochem. Soc., 164 (2017) A3804-A3813, https://doi.org/10.1149/2.0211714jes

[33] J. Chen, B.W. Yao, C. Li, G.Q. Shi, An improved Hummers method for eco-friendly synthesis of graphene oxide, Carbon, 64(2013)225-229, https://doi.org/10.1016/j.carbon.2013.07.055

[34] L. Chen, N. Li, M.X. Zhang, P.N. Li, Z.P. Lin, Effect of preparation methods on dispersion stability and electrochemical performance of graphene sheets, J. Solid State Chem., 249 (2017) 9-14, https://doi.org/10.1016/j.jssc.2017.01.009

[35] A. Rezaei, B. Kamali, A.R. Kamali, Correlation between morphological, structural and electrical properties of graphite and exfoliated graphene nanostructures, Measurement, 150(2020) 107087, https://doi.org/10.1016/j.measurement.2019.107087

[36] X.P. Gao, Y.L. An, W.S. Zhang, M.L. Yu, L.J. Ci, J.K. Feng, Self-supporting soft carbon fibers as binder-free and flexible anodes for high-performance sodium-ion batteries, Mater. Technol., 33 (2018) 810-814, https://doi.org/10.1080/10667857.2018.1509525

[37] X.Y. Li, J.K. Qu, H.W. Xie, Q.S. Song, G.F. Fu, H.Y. Yin, An electro-deoxidation approach to co-converting antimony oxide/graphene oxide to antimony/graphene composite for sodium-ion battery anode, Electrochim. Acta, 332 (2020) 135501, https://doi.org/10.1016/j.electacta.2019.135501

[38] W. Sun, Q. Sun, R.L. Lu, M.X. Wen, C. Liu, J.L. Xu, Y.X. Wu, Sodium hypophosphite-assist pyrolysis of coal pitch to synthesis P-doped carbon nanosheet anode for ultrafast and long-term cycling sodium-ion batteries, J. Alloy. Compd., 889 (2021) 161678, https://doi.org/10.1016/j.jallcom.2021.161678

[39] H. Sun, B. Liu, T. Peng, X. Zhao, Nitrogen-doped porous 3D graphene with enhanced supercapacitor properties, J. Mater. Sci., 53 (2018) 13100-13110, https://doi.org/10.1007/s10853-018-2561-4

[40] S. Sehar, F. Sher, S. Zhang, U. Khalid, E.C. Lima, Thermodynamic and kinetic study of synthesized graphene oxide-cuo nanocomposites: a way forward to fuel additive and photocatalytic potentials, J. Mol. Liq., 33 (2020) 113494, https://doi.org/10.1016/j.molliq.2020.113494

[41] Y. Hbiriq, M.R. Ammar, C. Fantini, L. Hennet, M. Zaghrioui, Probing symmetry-breaking defects in polished graphitizable sp2 carbons using angle-resolved polarized Raman scattering, Phys. Rev. B, 107 (2023) 134305, https://doi.org/10.1103/PhysRevB.107.134305

[42] A.R. Kamali, Nanocatalytic conversion of CO_2 into nanodiamonds, Carbon, 123 (2017) 205-215, https://doi.org/10.1016/j.carbon.2017.07.040

[43] J.Y. Zhang, Q. Zhang, X.L. Qu, G.B. Xu, B.Y. Fan, Z.H. Yan, F. Gui, L.W. Yang, Hierarchically pyridinic-nitrogen enriched porous carbon for advanced sodium-ion and lithium-sulfur batteries: Electrochemical performance and in situ Raman spectroscopy investigations, Appl. Surf. Sci., 574 (2022) 151559, https://doi.org/10.1016/j.apsusc.2021.151559

[44] S.J. Chen, K.J. Tang, F. Song, Z.C. Liu, N. Zhang, S.L. Lan, X.Q. Xie, Z.J. Wu, Porous hard carbon spheres derived from biomass for high-performance sodium/potassium-ion batteries, Nanotechnology, 33 (2021) 055401, https://doi.org/10.1088/1361-6528/ac317d

[45] M.D. Yan, Y.C. Qin, L.X. Wang, M.R. Song, D.D. Han, Q. Jin, S.J. Zhao, M.M. Zhao, Z. Li, X.Y. Wang, L. Meng, X.P. Wang, Recent Advances in Biomass-Derived Carbon Materials for Sodium-Ion Energy Storage Devices, Nanomaterials, 12 (2022) 930, https://doi.org/10.3390/nano12060930

[46] D.S. Knight, W.B. White, Characterization of diamond films by raman spectroscopy, J. Mater. Res., 4 (1989) 385-393, https://doi.org/10.1557/JMR.1989.0385

[47] A.R. Kamali, Green production of carbon nanomaterials in molten salts and applications, Diam. Relat. Mater., 83 (2018) 146-161, https://doi.org/10.1007/978-981-15-2373-1

[48] H.J. Seo, H. Kang, T. Lee, S. Chae, E. Kim, J.H. Lee, S.G. Lee, Correlation between redox

active sites and sodium storage behavior in dye/graphene nanohybrids, Appl. Surf. Sci., 587 (2022) 152859-152869, https://doi.org/10.1016/j.apsusc.2022.152859

[49] E.M. Lotfabad, J. Ding, K. Cui, A. Kohandehghan, W.P. Kalisvaart, M. Hazelton, D. Mitlin, High-Density Sodium and Lithium-Ion Battery Anodes from Banana Peels, ACS Nano, 8(2014), 7115-7129, http://doi.org/10.1021/nn502045y

[50] L.S. Severo, J.B. Rodrigues, D.A. Campanelli, V.M. Pereira, J.W. Menezes, E.W. de Menezes, C. Valsecchi, M.A. Vasconcellos, L.E. Armas, Synthesis and Raman characterization of wood sawdust ash, and wood sawdust ash-derived graphene, Diam. Relat. Mater., 117 (2021) 108496-108504, https://doi.org/10.1016/j.diamond.2021.108496

[51] L. Chang, Y.H. Hu, One-step synthesis of high surface-area honeycomb graphene clusters for highly efficient capacitive deionization, J. Phys. Chem. Solids, 134 (2019) 64-68, https://doi.org/10.1016/j.jpcs.2019.05.040

[52] J.W. Ben, Y.P. Jia, T. Wu, X.K. Liu, X.H. Li, Sodium birnessite@graphene hierarchical structures for ultrafast sodium ion storage, J. Electroanal. Chem., 906 (2022) 116007, https://doi.org/10.1016/j.jelechem.2021.116007

[53] P. Zhang, Y.R. Shu, Y. Wang, J.H. Ye, Y. Yang, Simple and efficient synthesis methods for fabricating anode materials of sodium-ion batteries and their sodium-ion storage mechanism study, J. Mater. Chem. A, 11 (2023) 2920-2932, https://doi.org/10.1039/d2ta09051a

[54] X.X. He, W.H. Lai, Y. Liang, J.H. Zhao, Z. Yang, J. Peng, X.H. Liu, Y.X. Wang, Y. Qiao, L. Li, X.Q. Wu, S.L. Chou, Achieving All-Plateau and High-Capacity Sodium insertion in Topological Graphitized Carbon, Adv. Mater., 35 (2023) 2302613, https://doi.org/10.1002/adma.202302613

[55] I. Sengupta, S. Chakraborty, M. Talukdar, S.K. Pal, S. Chakraborty, Thermal reduction of graphene oxide: how temperature influences purity, J. Mater. Res., 33(2018) 1-10, https://link.springer.com/article/10.1557/jmr.2018.338.

[56] C. Botas, P. Alvarez, P. Blanco, M. Granda, C. Blanco, R. Santamaria, L.J. Romasanta, R. Verdejo, M.A. Lopez-Manchado, R. Menendez, Graphene materials with different structures prepared from the same graphite by the Hummers and Brodie methods, Carbon,

65 (2013) 156-164, https://doi.org/10.1016/j.carbon.2013.08.009

[57] Y.J. Huang, J.Y. Wu, X.T. Xiao, W.H. Deng, Y.S. Bai, X.Q. Bai, Y.C. Yang, G.Q. Zou, T.J. Wu, H.S. Hou, M.J. Jing, X.B. Ji, Multivalent manganese-based composite materials for sodium energy storage in ether electrolyte, J. Power Sources, 588 (2023) 233742, https://doi.org/10.1016/j.jpowsour.2023.233742

[58] A.M. Abdelkader, C. Valles, A.J. Cooper, I.A. Kinloch, R.A.W. Dryfe, Alkali Reduction of Graphene Oxide in Molten Halide Salts: Production of Corrugated Graphene Derivatives for High-Performance Supercapacitors, ACS Nano., 8 (2014) 11225-11233, https://doi.org/10.1021/nn505700x

[59] Y.H. Kim, G.W. Lee, Y.J. Choi, K.B. Kim, In Situ Growth of Novel Graphene Nanostructures in Reduced Graphene Oxide Microspherical Assembly with Restacking-Resistance and Inter-Particle Contacts for Energy Storage Devices, Small, 17 (2021) 2101930, https://doi.org/10.1002/smll.202101930

[60] M.D. Slater, D.H. Kim, E. Lee, C.S. Johnson, Sodium-Ion Batteries, Adv. Funct. Mater., 23 (2013)947-958, https://doi.org/10.1002/adfm.201200691

[61] J.H. Sun, M. Sadd, P. Edenborg, H. Gronbeck, P.H. Thiesen, Z.Y. Xia, V. Quintano, R. Qiu, A. Matic, V. Palermo, Real-time imaging of Na+ reversible intercalation in “Janus” graphene stacks for battery applications, Sci. Adv., 7 (2021) eabf0812, https://doi.org/10.1126/sciadv.abf0812

[62] Y. Wu, X.C. Wang, F. Zhang, L.J. Hai, Q.H. Chen, C.Q. Chao, A.K. Yang, Y. Sun, D.Z. Jia, Combining Janus Separator and Organic Cathode for Dendrite-Free and High-Performance Na-Organic Batteries, Adv. Funct. Mater., 1(2023) 2309552, https://doi.org/10.1002/adfm.202309552

[63] S.Y. Li, H.J. Wu, C.J. Wu, M. Jin, H. Yi, S.Y. Lu, Y. Zhang, 4,4′-Biphenyldicarboxylic acid as an anode for sodium-ion batteries: Different electrochemical behaviors in ester and ether-based electrolytes, J. Electroanal. Chem., 950 (2023) 117852, https://doi.org/10.1016/j.jelechem.2023.117852

[64] Z.Q. Song, M.X. Di, S.H. Chen, Y. Bai, Three-dimensional N/O co-doped hard carbon anode enabled superior stabilities for sodium-ion batteries, Chem. Eng. J., 470 (2023) 144237, https://doi.org/10.1016/j.cej.2023.144237

[65] J.J. Zeng, T. Wang, X.R. Gu, H.D. Zhu, C.W. Xu, D.D. Sun, C. Ge, R. Ding, J. Li, J.G. Liu, Nickel-templated carbon foam anodes for sodium-ion batteries, FlatChem., 40 (2023) 100508, https://doi.org/10.1016/j.flatc.2023.100508

[66] M.K. Shehab, K.S. Weeraratne, T. Huang, K.U. Lao, H.M. El-Kaderi, Exceptional Sodium-Ion Storage by an Aza-Covalent Organic Framework for High Energy and Power Density Sodium-Ion Batteries, ACS Appl. Mater. Interfaces, 13 (2021) 15083-15091, https://doi.org/10.1021/acsami.0c20915

[67] H.Y. Fu, B. Gao, Y. Qiao, W.H. Zhu, Z. Liu, G.Y. Wei, Z.B. Feng, A.R. Kamali. Graphene nanonetwork embedded with polyaniline nanoparticles as anode of Li-ion battery, Chem. Eng. J., 477 (2023) 146936, https://doi.org/10.1016/j.cej.2023.146936

[68] G.R. Yang, Z.Y. Zhou, X.F. Liu, Y. Zhang, S.L. Wang, W. Yan, S.J. Ding, Bowl-shaped hollow carbon wrapped in graphene grown in situ by chemical vapor deposition as an advanced anode material for sodium ion batteries, J. Colloid Interface Sci., 637 (2023) 283-290, https://doi.org/10.1016/j.jcis.2023.01.092

[69] H.T. Xue, Q. Sun, R.F. Lu, C. Liu, Pyrolysis of coal pitch-infused melamine foam to construct N-doped carbon anodes for high-performance sodium-ion battery, J. Electroanal. Chem., 902 (2021) 115809, https://doi.org/10.1016/j.jelechem.2021.115809

[70] X.J. Xu, J. Liu, J.W. Liu, L.Z. Ouyang, R.Z. Hu, H. Wang, L.C. Yang, M. Zhu, A General Metal-Organic Framework (MOF)-Derived Selenidation Strategy for In Situ Carbon-Encapsulated Metal Selenides as High-Rate Anodes for Na-Ion Batteries, Adv. Funct. Mater., 28 (2018) 1707573, https://doi.org/10.1002/adfm.201707573

[71] N. Sun, Z. Guan, Y. Liu, Y. Cao, Q. Zhu, H. Liu, Z. Wang, P. Zhang, B. Xu, Extended "Adsorption-Insertion" Model: A New Insight into the Sodium Storage Mechanism of Hard Carbons, Adv. Energy Mater., 9 (2019) 1901351, https://doi.org/10.1002/aenm.201901351

[72] D.A. Stevens, J.R. Dahn, The mechanisms of lithium and sodium insertion in carbon materials, J. Electrochem. Soc., 148 (2001) A803-A811, https://doi.org/10.1149/1.1379565

[73] Y.L. Cao, L.F. Xiao, M.L. Sushko, W. Wang, B. Schwenzer, J. Xiao, Z.M. Nie, L.V. Saraf, Z.G. Yang, J. Liu, Sodium ion insertion in hollow carbon nanowires for battery

applications, Nano Lett., 12 (2012) 3783-3787, https://doi.org/10.1021/nl3016957

[74] S. McArdle, F. Bauer, S.F. Granieri, M. Ast, F.D. Fonzo, A.T. Marshall, H. Radinger, Defective carbon for next-generation stationary energy storage systems: sodium-ion and vanadium flow batteries, ChemElectroChem, 11 (2024) e202300512, https://doi.org/10.1002/celc.202300512

[75] B.A. Zhang, C.M. Ghimbeu, C. Laberty, C. Vix-Guterl，J. M. Tarascon, Correlation between microstructure and Na storage behavior in hard carbon, Adv. Energy Mater., 6 (2016) 1501588, https://doi.org/10.1002/aenm.201501588

[76] Y.M. Li, Y.S. Hu, M.M. Titirici, L.Q. Chen, X.J. Huang, Hard carbon microtubes made from renewable cotton as high-performance anode material for sodium-ion batteries, Adv. Energy Mater., 6 (2016) 1600659, https://doi.org/10.1002/aenm.201600659

[77] C. Bommier, T.W. Surta, M. Dolgos, X.L. Ji, New mechanistic insights on Na-ion storage in no graphitizable carbon, Nano Lett., 15 (2015) 5888-5892, https://doi.org/10.1021/acs.nanolett.5b01969

[78] M. Wahid, D. Puthusseri, Y. Gawli, N. Sharma, Hard Carbons for Sodium-Ion Battery Anodes: Synthetic Strategies, Material Properties, and Storage Mechanisms, ChemSusChem, 11 (2018) 506-526, https://doi.org/10.1002/cssc.201701664

[79] G.Z. Fang, Q.C. Wang, J. Zhou, Y.P. Lei, Z.X. Chen, Z.Q. Wang, A.Q. Pan, S.Q. Liang, Metal Organic Framework-Templated Synthesis of Bimetallic Selenides with Rich Phase Boundaries for Sodium-Ion Storage and Oxygen Evolution Reaction, ACS Appl. Nano Mater., 13 (2019) 5635-5645, https://doi.org/10.1021/acsnano.9b00816

[80] D. Ledwoch, J.B. Robinson, D. Gastol, K. Smith, P.R. Shearing, D.J.L. Brett, E. Kendrick, Hard Carbon Composite Electrodes for Sodium-Ion Batteries with Nano-Zeolite and Carbon Black Additives, Batteries Supercaps, 4 (2021) 163-172, https://doi.org/10.1002/batt.202000161

[81] N. Li, Q.Y. Yang, Y.X. Wei, R.C. Rao, Y.P. Wang, M.L. Sha, X.H. Ma, L.L. Wang, Y.T. Qian, Phosphorus-Doped Hard Carbon with Controlled Active Groups and Microstructure for High-Performance Sodium-Ion Batteries, J. Mater. Chem. A, 8 (2020) 20486-20492, https://doi.org/10.1039/D0TA06910H

[82] Y. Zhang, H. Tao, L. Huang, M. Liu, W. Shi, Nitrogen and Sulfur Co-Doped Mesoporous

Carbon for Sodium Ion Batteries, ACS Appl. Nano Mater., 2 (2019) 5643-5654. https://doi.org/10.1021/acsanm.9b01178

[83] W. Yang, K. He, Y.J. Zhu, F.D. Han, Y.H. Xu, I. Matsuda, Y. Ishii, J. Cumings, C.S. Wang, Expanded graphite as superior anode for sodium-ion batteries, Nat. Commun., 5 (2014) 4033, https://doi.org/10.1038/ncomms5033

[84] L. David, G. Singh, Reduced Graphene Oxide Paper Electrode: Opposing Effect of Thermal Annealing on Li and Na Cyclability, J. Phys. Chem. C, 118 (2014) 28401-28408, https://doi.org/10.1021/jp5080847

[85] J. Ding, H. Wang, Z. Li, A. Kohandehghan, K. Cui, Z. Xu, B. Zahiri, X. Tan, E.M. Lotfabad, B.C. Olsen, D. Mitlin, Carbon Nanosheet Frameworks Derived from Peat Moss as High-Performance Sodium Ion Battery Anodes, ACS Nano, 7 (2013) 11004-11015, https://doi.org/10.1021/nn404640c

[86] J. Zhao, Y.Z. Zhang, F. Zhang, H.F. Liang, F.W. Ming, H.N. Alshareef, Z.Q. Gao, Partially Reduced Holey Graphene Oxide as High-Performance Anode for Sodium-Ion Batteries, Adv. Energy Mater., 9 (2019) 1803215, https://doi.org/10.1002/aenm.201803215

[87] S. Li, J. Qiu, C. Lai, M. Ling, H. Zhao, S. Zhang, Surface capacitive contributions: Towards high-rate anode materials for sodium ion batteries, Nano Energy, 12 (2015) 224-230, https://doi.org/10.1016/j.nanoen.2014.12.032

[88] A. Alzharani, M.K. Shehab, D.D. Rodene, J.U. Ahmed, A.M. Bakry, M.M. Kaid, H.M. El-Kaderi, Surface Modification of Partially Reduced Graphene Oxide for Advanced Electrode Material in Rechargeable Sodium Batteries, Energy Fuels, 36 (2022) 4967-4977, https://doi.org/10.1021/acs.energyfuels.2c00193

[89] S.L. Zhang, J.J. He, J. Zheng, C.S. Huang, Q. Lv, K. Wang, N. Wang, Z.G. Lan, Porous graphdiyne applied for sodium ion storage, J. Mater. Chem. A, 5 (2017) 2045-2051, https://doi.org/10.1039/C6TA09822C

[90] J.T. Xu, M. Wang, N.P. Wickramaratne, M. Jaroniec, S.X. Dou, L.M. Dai, High-Performance Sodium Ion Batteries Based on a 3D Anode from Nitrogen-Doped Graphene Foams, Adv. Mater., 27 (2015) 2042-2048, https://doi.org/10.1002/adma.201405370

[91] J. Sun, H.W. Lee, M. Pasta, H.T. Yuan, G.Y. Zheng, Y.M. Sun, Y.Z. Li, Y. Cui, A phosphorene–graphene hybrid material as a high-capacity anode for sodium-ion batteries,

Nat. Nanotechnol., 10 (2015) 980-985, https://doi.org/10.1038/NNANO.2015.194

[92] Z.X. Li, T.J. Hu, J. Yang, X. Yu, F.Y. Su, Q.X. Bai, Y.Y. Ma, Y. C. Song, M. Jia, X.Y. Zhou, J.J. Tang, In Situ Constructing of Rigid-Soft Coupling Solid–Electrolyte Interphase on Silicon Electrode toward High-Performance Lithium-Ion Batteries, Small, 9 (2023) 2305991, https://doi.org/10.1002/smll.202305991

[93] J.Y. Wan, F. Shen, W. Luo, L.H. Zhou, J.Q. Dai, X.G. Han, W.Z. Bao, Y. Xu, J. Panagiotopoulos, X.X. Fan, D. Urban, A.M. Nie, R. Shahbazian-Yassar, L.B. Hu, In Situ Transmission Electron Microscopy Observation of Sodiation−Desodiation in a Long Cycle, High-Capacity Reduced Graphene Oxide Sodium-Ion Battery Anode, Chem. Mater., 28 (2016) 6528-6535, https://doi.org/10.1021/acs.chemmater.6b01959

[94] Y. Liu, F.F. Fan, J.W. Wang, Y. Liu, H.L. Chen, K.L. Jungjohann, Y.H. Xu, Y.J. Zhu, D. Bigio, T. Zhu, C.S. Wang, In Situ Transmission Electron Microscopy Study of Electrochemical Sodiation and Potassiation of Carbon Nanofibers, Nano Lett., 14 (2014) 3445-3452, https://doi.org/10.1021/nl500970a

[95] Z.L. Xu, J. Park, G. Yoon, H. Kim, K. Kang, Graphitic Carbon Materials for Advanced Sodium-Ion Batteries, Small Methods, 3 (2019) 1800227, https://doi.org/10.1002/smtd.201800227

[96] Y. Fang, D. Luan, Y. Chen, S. Gao, X.W.D. Lou, Rationally Designed Three-Layered Cu2S@Carbon@MoS2 Hierarchical Nanoboxes for Efficient Sodium Storage, Angew. Chem., Int.Ed.,59(2020) 7178-7183, https://doi.org/10.1002/anie.201915917

[97] F. Sun, H. Wang, Z.B. Qu, K.F. Wang, L.J. Wang, J.H. Gao, J.M. Gao, S.Q. Liu, Y.F. Lu, Carboxyl-Dominant Oxygen Rich Carbon for Improved Sodium Ion Storage: Synergistic Enhancement of Adsorption and Intercalation Mechanisms, Adv. Energy Mater., 11(2021) 2002981, https://doi.org/10.1002/aenm.202002981

[98] H. Jia, N. Sun, M. Dirican, Y. Li, C. Chen, P. Zhu, C. Y. Yan, J. Zang, J. S. Guo, J. S. Tao, J. S. Wang, F. C. Tang, X. W. Zhang, Electrospun Kraft Lignin/Cellulose Acetate-Derived Nanocarbon Network as an Anode for High-Performance Sodium-Ion Batteries, ACS Appl. Mater. Interfaces,10(2018)44368-44375, https://doi.org/10.1021/acsami.8b13033

[99] J.N. Lu, Z. Zhang, Y.F. Zheng, Y.H. Gao, In Situ Transmission Electron Microscopy for Sodium-Ion Batteries, Adv. Mater., 29 (2023) 2300359,

https://doi.org/10.1002/adma.202300359